

# Metamaterial Structural Design: Creating optical-frequency metamaterials with plasmonic nano-particle arrangements and generating unit cells with evolutionary algorithms

---

Thesis presented by:

Carlos Andres Esteva

Approved by:

---

Dr. Andrea Alu

---

Dr. Dean Neikirk

The University of Texas at Austin

Sandia National Laboratories



## *Dedication*

I dedicate this thesis to my family, for their continued support and encouragement throughout my life and education.

I further dedicate this thesis to Dr. Andrea Alu, for his inspirational teaching, guidance, and thesis supervision in my latter years as an undergraduate, and Dr. Michael B. Sinclair, for his excellent mentorship and supervision during this thesis work.

In addition, I would like to acknowledge Dr. Dean Neikirk, for inspiring me to pursue electromagnetics as an area of specialization, and Dr. Phil Anderson, my high school physics teacher, for motivating me to excel as an undergraduate.

Finally, many thanks to everyone that has made a positive impact on my life and undergraduate career – to all my friends, peers, and co-workers.

Thank you all.

## *Abstract*

Metamaterials are artificial structures which can manipulate electromagnetic (EM) waves at will. These periodic lattices give engineers and researchers a large degree of control over EM radiation and can be used to create exciting and novel applications such as invisibility cloaks, superlenses, and devices with negative indices of refraction.

The geometrical design of these structures is a large challenge in creating them. These structures are periodic lattices with magnetodielectric, metallic, or plasmonic inclusions. Their size, which scales on the order of the wavelength of interest, and their geometry uniquely determine the effect on EM waves as well as the frequency bands in which they operate.

We present in this thesis the development of a bi-directional computational platform for metamaterial structural design. This platform serves to extract, from a given geometry, the bulk material properties of the corresponding metamaterial. It further serves to generate metamaterial unit cells which satisfy pre-determined sets of material parameters.

This work is split between The University of Texas at Austin and Sandia National Laboratories

### UT-Austin

Optical frequency metamaterials are particularly challenging to create due both to their nano-scale size and the fact that the EM response of conventional materials changes at these frequencies. This thesis explores the use of plasmonic sphere nano-particles and core-shell structures as inclusions for optical frequency metamaterials. Their ease of manufacturing and isotropic geometry make them of interest to this work, and we hypothesize that they are effective at generating metamaterials in these frequency ranges. This work concludes that these nano-spheres can act as metamaterials in certain arrangements, while not in others. It further encourages the continued investigation of plasmonic-dielectric core-shell particles, providing inconclusive evidence of their metamaterial nature.

### Sandia National Labs

Non-homogenous metamaterial structures in the infrared domain require the automation of unit-cell generation. In order to achieve spatially varying bulk parameters the unit cell geometries must change in space. To achieve this requires an automation scheme which takes as input desired material parameters and generates a unit cell that yields those parameters. This thesis investigates the use of evolutionary algorithms to optimize metamaterial unit cells. We create a parameter space whose vector valued points represent potential unit cells and use these algorithms to optimize unit cell geometries based on a pre-defined metric, such as their bulk material response.

## Table of Contents

Chapter 1 : Introduction .....	7
A. Metamaterials .....	9
B. Applications .....	10
C. Motivation/Objectives .....	12
Chapter 2 : METAMATERIAL GEOMETRY ANALYSIS (University of Texas at Austin) .....	13
A. Development of COMSOL/MATLAB Interface for periodic full-wave simulation.....	15
Weak Form Formulation .....	15
2D Eigenvalue Problem – Normal Incidence .....	16
2D Eigenvalue Problem – Oblique Incidence .....	23
B. Dielectric Sphere.....	24
COMSOL/MATLAB Formulation.....	25
Dispersion Analysis .....	25
C. Plasmonic Spheres .....	27
Isotropic Case .....	27
Linear Chain Case.....	29
Planar Array Case.....	30
Arrangement Comparison.....	32
D. Core-Shell Structure.....	34
Results.....	35
E. Conclusions.....	36
Chapter 3 METAMATERIAL GEOMETRY GENERATION (Sandia National Laboratories) .....	37
A. Intro/Motivation.....	37
B. Evolutionary Algorithms.....	38
Genetic Algorithm.....	38
Simulated Annealing.....	39
C. Geometry Representation in Parameter Space.....	41
D. Geometry Evolution .....	42
Fitness Functions – Shape Morphing.....	42
Fitness Functions – Metamaterial Generation .....	44
E. Conclusions.....	45

Chapter 4 Future Work/Conclusions .....	46
A. Analysis of Conjugate SRRs using COMSOL/MATLAB Platform .....	46
B. Automated Metamaterial Geometry Generation .....	46
C. Conclusions.....	47
References .....	48

## List of Figures

Figure 1.1: Electromagnetic Spectrum (www.lbl.gov).....	7
Figure 1.2: Devices that interact with signals .....	7
Figure 1.3: Molecular wave interaction.....	8
Figure 1.4: Electric and Magnetic Field Effects .....	8
Figure 1.5: Negative refraction index material (www.macdiarmid.ac.nz) .....	9
Figure 1.6: Negative-Index Material Superlens (scientopia.org) .....	11
Figure 1.7: Metamaterial Invisibility Cloak [5] .....	11
Figure 2.1: 1D Metamaterial. Circular inclusions in a square linear chain .....	13
Figure 2.2: 3D Metamaterial. Square split-ring resonators suspended in a lattice[8] .....	13
Figure 2.3: 2D Metamaterial. Circular Split ring resonators and wire rods held up on a platform (Smith and Schultz, UCSD) .....	13
Figure 2.4: Eigenmodal propagation in a rectangular waveguide .....	14
Figure 2.5: 2D Eigenvalue Problem Geometry. Dielectric Cylinder with $\epsilon_r=10$ , $\mu_r=1$ , radius $a = 0.2$ cm, side length $d = 1$ cm.....	17
Figure 2.6: Tetrahedral and Quadratic Meshing Schemes .....	18
Figure 2.7: H Field distribution for propagating mode $f = 0.143$ and $k = 0.438$ .....	18
Figure 2.8: Dispersion diagram for wave propagation in the x direction for a 2D metamaterial composed of a dielectric cylinder inside a square unit cell. ....	20
Figure 2.9: H field distribution near the first cutoff $f = 0.764$ and $k=2.78$ .....	21
Figure 2.10: Evanescent Mode in band gap at $f = 1.1$ , $k = \pi +0.9i$ .....	21
Figure 2.11: H field distribution for a propagating mode at $f = 1.3$ and $k = 2.57$ .....	22
Figure 2.12: H field distribution at the top of the first Brillouin Zone. $f = 1.67$ , $k = 0.42$ .....	23
Figure 2.13: 2D Dielectric Cylinder Oblique Incidence $30^\circ$ .....	23
Figure 2.14: 2D Cylinder - Oblique Incidence at $60^\circ$ .....	24
Figure 2.15: Dielectric Sphere .....	25
Figure 2.16: 3D Dielectric Sphere Dispersion Curves – COMSOL.....	26
Figure 2.17: 3D Dielectric Sphere Dispersion Curves - CST.....	26
Figure 2.18: Isotropic Sphere .....	28
Figure 2.19: Isotropic Plasmonic Sphere Dispersion .....	28
Figure 2.20: Linear Chain Plasmonic Sphere Arrangement .....	29
Figure 2.21: Linear Chain Dispersion .....	30

Figure 2.22: Planar Array Plasmonic Sphere .....	31
Figure 2.23: Planar Array Dispersion .....	31
Figure 2.24: Dispersion of Plasmonic Sphere Arrangements.....	32
Figure 2.25: Analytical Results – Dispersion of Plasmonic Sphere Arrangements.....	33
Figure 2.26: Zoomed-in Dispersion of Planar Array and Linear Chain Arrangements.....	34
Figure 2.27: Core-Shell Structure .....	35
Figure 2.28: Analytical Dispersion Curve – Core-Shell Structure .....	35
Figure 2.29: COMSOL Dispersion Curve - CoreShell Structure.....	36
Figure 3.1: Transformation Optics - transforming a coordinate system .....	37
Figure 3.2: Diagram of Genetic Algorithm Evolution .....	39
Figure 3.3: Local Maxima in a parameter space .....	40
Figure 3.4: Randomness of Transitioning in Simulated Annealing.....	41
Figure 3.5: Unit Cell Pixilation .....	42
Figure 3.6: Simulated Annealing - Morph to Shape .....	44
Figure 3.7: Eiger - Computational Far-Field solver .....	44
Figure 3.8: Computational Solver - Material properties to metamaterial geometry.....	45
Figure 4.1: Dual Split-Ring Resonator.....	46
Figure 4.2: Bi-directional Platform for Metamaterial Design and Analysis .....	47

## Chapter 1 : Introduction

Propagating electromagnetic (EM) radiation is composed of oscillating electric and magnetic fields. These signals form what is known as the electromagnetic spectrum – the range of all possible frequencies ( $\omega$ ) of electromagnetic radiation. The amplitude of these fields determines their relative strength, and their frequency determines where they lie in the spectrum. The wavelength of this radiation is the length of one oscillation and is defined as  $\lambda=2\pi/\omega$ .

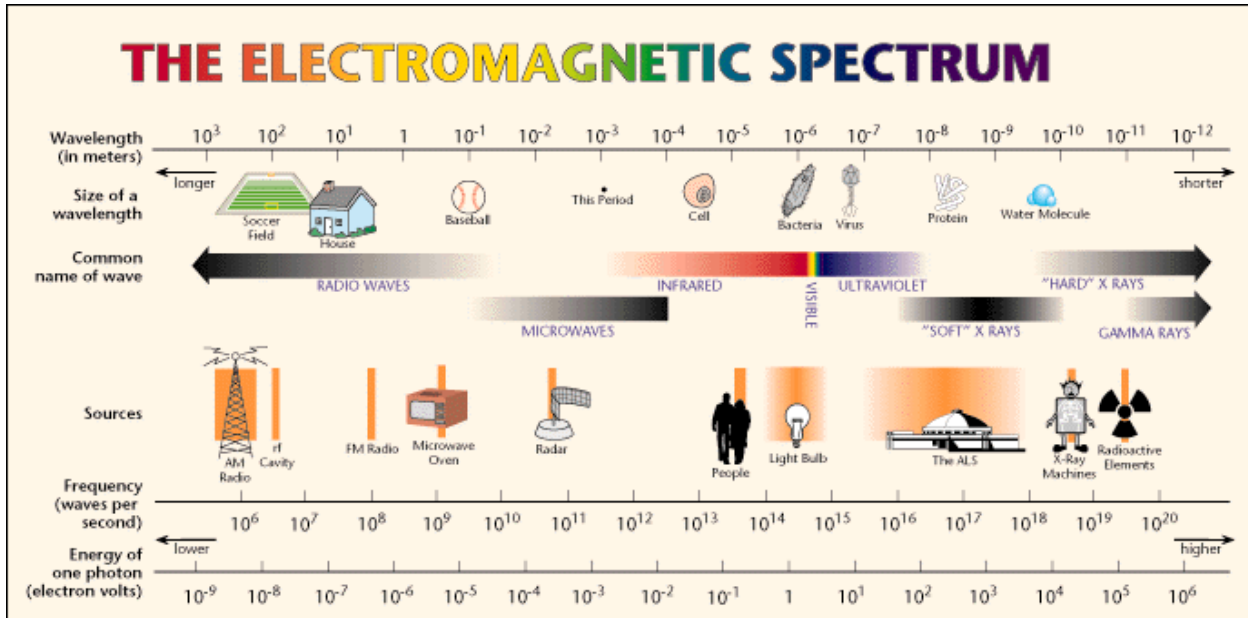


Figure 1.1: Electromagnetic Spectrum  
([www.lbl.gov](http://www.lbl.gov))

The different parts of the spectrum, from radio waves at the long wavelength limit to gamma rays on the right in Figure 1.1, above, each serve different purposes and can be used for various applications. Radiowaves are commonly manipulated for telecommunications, cell phones, and AM/FM radio. Infrared is well known to be effective in night-imaging applications, since humans eyes cannot see this wavelength. Visible light frequencies occupy the bulk of the sun's spectral profile (reference something) and thus form the frequency band that most animals have evolved to detect with their eyes. Continuing up the frequency spectrum, X-rays have medical applications and gamma rays are best describes by quantum mechanical effects and are useful in understanding nuclear physics.

Figure 1.2: Devices that interact with signals



Our ability to utilize the electromagnetic spectrum in science and technology relies on the way that these signals interact with materials. Devices such as cell phones, antennas, and WIFI routers all use materials to manipulate and control EM signals.

When an EM wave enters a material, it automatically changes its properties. The degree of modification is a function of the material as well as the frequency of the impinging wave. Engineers can leverage this quality to create such devices.

In addition, we can characterize the particular way in which a material will interact with a wave. As is shown schematically in Figure 1.3, when a wave (red line) enters a material, its oscillating electric and magnetic fields interact with the material's molecules.

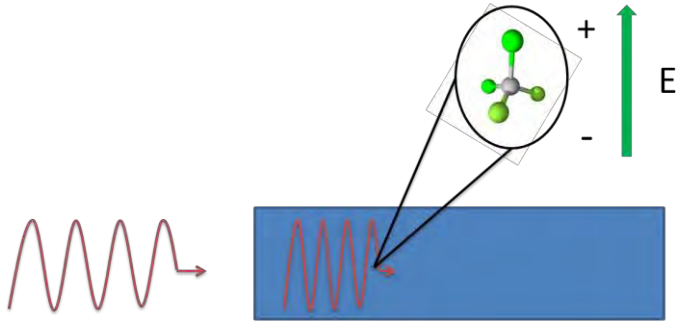


Figure 1.3: Molecular wave interaction

This interaction can lead to power loss, field perturbations, a change in the effective frequency of propagation, and other such effects.

In particular, we can describe the way in which the electric and magnetic fields act on these molecules. Electric fields create dipoles (and other higher-order multiples) and cause protons and

electrons to become polarized and move away from each other. Magnetic fields, on the other hand, induce loops of circulating current which act as magnetic dipoles. The electric permittivity  $\epsilon$  and the magnetic permeability  $\mu$  describe this interaction. We denote the permittivity of free space to be  $\epsilon_0$  and the permeability of free space to be  $\mu_0$ . Then in free space we have that the electric displacement field vector is  $D \triangleq \epsilon_0 E$  where  $E$  is the electric field vector. The magnetic displacement field vector is  $B \triangleq \mu_0 H$  where  $H$  is the magnetic field vector.

In a material with an EM response, we denote  $P$ , the polarization vector, to be the effect of the  $E$  field on these molecules. Then if  $\epsilon$  is the permittivity of the material we see that

$$D = \epsilon E = \epsilon_0 E + P \Rightarrow P = (\epsilon - \epsilon_0) E$$

and similarly we have that,

$$B = \mu H = \mu_0 H + M \Rightarrow M = (\mu - \mu_0) H$$

where  $M$  is the magnetization vector. It is worth mentioning here, although outside the scope of this thesis, that we can further characterize the degree to which  $E$  induced  $M$  and  $H$  induced  $P$  by writing

$$D = \epsilon E + \alpha H$$

$$B = \mu H + \beta E$$

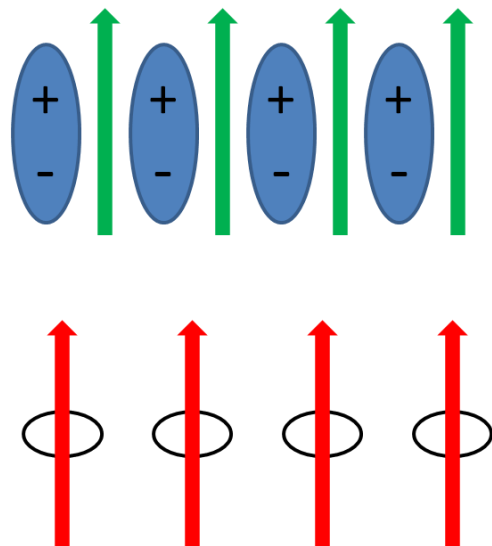


Figure 1.4: Electric and Magnetic Field Effects

## A. Metamaterials

Metamaterials differ from regular materials in their anomalous and exotic material responses. In most naturally occurring materials both the permittivity and permeability must be greater than that of free space. There are a few naturally occurring materials that exhibit  $\epsilon < \epsilon_0$  or  $\mu < \mu_0$ , but there exists no (known) material which exhibits both.

Metamaterials are artificial structures with variable  $\epsilon$  and  $\mu$  that can achieve  $\epsilon < \epsilon_0$  and  $\mu < \mu_0$ . We call this a double negative (DNG) material. It has been shown that such a material exhibits truly unique properties in its interaction with EM waves, such as negative index of refraction [1].

As a propagating ray passes from one medium to another (Figure 1.5), it has a tendency to bend away from or towards the boundary normal (dotted line) upon entering a double positive material (DPS) possessing  $\epsilon > \epsilon_0$ ,  $\mu > \mu_0$ . This bending, called refraction, follows Snells law:

1.1

$$\frac{\sin(\theta_i)}{\sin(\theta_t)} = \frac{n_t}{n_i}$$

$$n = \sqrt{\epsilon\mu}$$

where  $\theta_i$  and  $\theta_t$  denote the angle of incidence and angle of transmission, respectively, relative to the boundary normal, and  $n_i$  and  $n_t$  are the indices of refraction of the incidence medium and transmitted medium, respectively.

In a DNG metamaterial, however,  $n = -\sqrt{\epsilon\mu}$ , resulting in negative refraction and light bending *away* from the boundary normal. Note that this still satisfies Snells law.

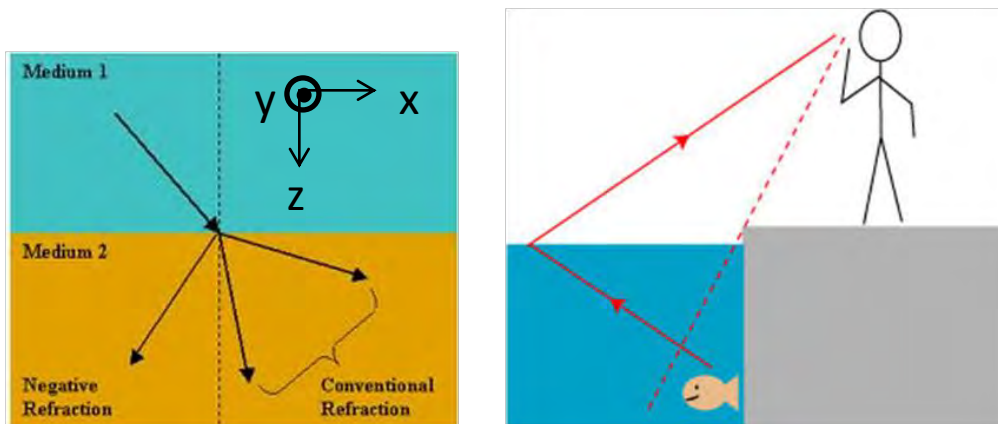


Figure 1.5: Negative refraction index material ([www.macdiarmid.ac.nz](http://www.macdiarmid.ac.nz))

Effectively this means that if you are an observer standing on the edge of a pool filled with liquid metamaterial, you would be able to see a fish hidden in the corner of the pool.

Another exciting phenomenon in DNG metamaterials is the fact that propagation in a metamaterial occurs opposite to the direction of power flow. These backward-waves are a result of power conservation and conservation of momentum at the boundary of refraction. Let medium 1 be a DPS material, medium 2 be DNG, and let a wave propagating in this material, following Figure 1.5, be described as

$$1.2 \quad \begin{aligned} \mathbf{E} &= \overline{E}_0 e^{-j(\omega t - \vec{k} \cdot \vec{r})} \\ \mathbf{H} &= \frac{\mathbf{k} \times \overline{E}_0}{\eta_0} e^{-j(\omega t - \vec{k} \cdot \vec{r})} \end{aligned}$$

where  $E_0$  is the wave amplitude and oscillation vector,  $\eta_0 = \sqrt{\mu_0 / \epsilon_0}$  is the wave impedance,  $t$  is time,  $\vec{r}$  is a Cartesian directional vector, and  $\mathbf{k}$  is the wave vector  $\vec{k} = (k_x, k_y, k_z)$

This wave travels in the +z direction and carries power in the +z direction. When it enters medium 2 from medium 1, the tangential component of the wave vector,  $k_x$ , must be conserved across the interface in order to ensure conservation of momentum. Since  $n < 0$ , however, the angle of transmission will be negative and thus the longitudinal component of the wavenumber in medium 2 will also be negative (i.e.  $k_{z,transmitted} < 0$ ). Power conservation ensures that power continues to flow in the positive z direction, but now the wavenumber in medium 2 ( $\beta$ ) is opposite in sign to power flow. This, in effect, is a backward wave.

The group velocity is the rate at which information can be transmitted through a signal, and it can be shown to be [2]

$$1.3 \quad v_g = \frac{\partial \omega}{\partial \beta}$$

A key component of metamaterials, and one which will be studied extensively later in this thesis, is the fact that this group velocity is negative in a metamaterial. This means it is opposite in sign to the direction of the phase  $\beta$ , and thus opposite in sign to the phase velocity

$$1.4 \quad v_p = \frac{\omega}{\beta}$$

## B. Applications

So how might we leverage these phenomena to develop metamaterial applications? We just described how metamaterials exhibit a negative index of refraction and backward propagating waves. In a groundbreaking paper in 2001, Sir John Pendry showed that a metamaterial slab with permittivity and permeability opposite in sign to those of free-space made a perfect lens.[3]

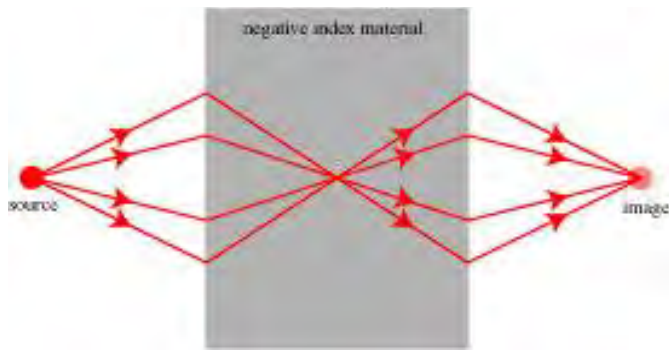


**Figure 1.6: Negative-Index Material Superlens** (<http://skullsinthestars.com/2009/11/20/reversing-optical-shockwaves-using-metamaterials/>)

An entering wave would refract twice, at both interfaces, and be focused onto an image point on the opposite side of the lens (Figure 1.6). What is truly remarkable about this lens is that it goes beyond the diffraction limit. Any wave emitted or scattered by the source that impinges upon the lens will be fully refracted into the material and transferred to the image point. Conventional optics lenses cannot accomplish this since a wave incident on a DPS boundary at a large enough angle risks total internal reflection. In addition, an evanescent wave (exponentially decaying wave:  $\vec{k} \in \mathbb{C}$ ) which would normally be lost in conventional imaging is actually transmitted through this lens. Strong resonant modes on the second boundary boost up the decaying wave to the point where its amplitude at the image point equals its amplitude at the source.

Another exciting application using metamaterials is the invisibility cloak. It has been shown theoretically and experimentally [4] that by wrapping a metamaterial cloak around an object, it is possible to bend impinging radiation around an object and get this radiation to converge on the opposite side, rendering it invisible.

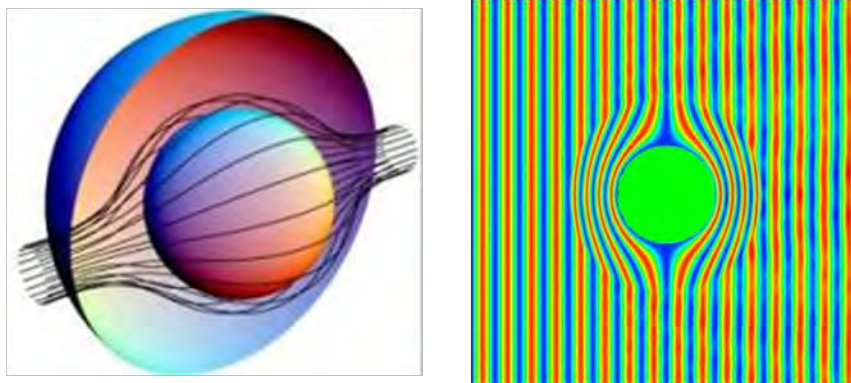


**Figure 1.7: Metamaterial Invisibility Cloak** [5], [6]

A different type of cloak has also been demonstrated. Instead of bending radiation around an object, this cloak effectively “cancels out” the scattered radiation from a small object [6]. While the first cloak requires a non-homogeneous metamaterial shell, this second kind requires a homogenous one, rendering it much easier to fabricate in practice.

## C. Motivation/Objectives

It is of great interest to researchers to create metamaterials at optical frequencies. Optical frequency superlenses could revolutionize biomedical imaging, for instance, and a very broadband optical frequency cloaks could render objects invisible to human eyes.

As will be describes in more intricate detail in the following chapter, metamaterials are not composite materials, but structures. In particular, they are periodic arrays of inclusions suspended in a lattice. These lattices scale on the order of the wavelength, and a metamaterial lattice period  $d$  must satisfy the quasi-static limit  $d < \lambda / 10$ . We can thus consider the excitation of the cell to be nearly uniform and describe this lattice as a bulk material (like a composite) by applying various homogenization schemes [7].

Given this size constraint, building an optical frequency metamaterial would require a lattice period no larger than 75nm. At this scale, not only does fabrication become a challenge, but conventional materials such as metals and dielectrics change in their EM response. For instance, at long wavelengths metals act as very good, low-loss conductors, with very high permittivity. However at optical frequencies these metals become plasmonic, with a permittivity that may be described as  $\varepsilon(\omega) = \varepsilon_0(1 - 3(\omega_p / \omega)^2)$ . An additional issue with optical frequencies is the lack of natural magnetic response. Most materials exhibit little to no magnetic response when interacting with optical frequency radiation.

**This thesis seeks to investigate several questions.**

- 1) Can we use plasmonic nano-spheres to create optical-frequency metamaterials?**
- 2) Can we induce a magnetic response at optical frequencies by combining plasmonic spheres with dielectric shells?**
- 3) Can we use computer algorithms to generate viable metamaterials given a material's desired EM response?**

The first two questions were investigated at The University of Texas at Austin in the research lab of Dr. Andrea Alu. We developed a computational platform which allows us to rigorously describe a unit cell's interaction with an impinging plane wave and extract its bulk material parameters. This allows us to determine if a given geometry can act as a metamaterial. By applying this platform to plasmonic sphere arrangements and a core-shell structure composed of a plasmonic sphere core and a dielectric shell, we determined if these geometries functioned as metamaterials, and for what frequency bands.

The third question has been investigated at Sandia National Laboratories in division 1816: Electronic and Nanostructure, under the supervision of Dr. Michael B. Sinclair. We generated a parameter-space in which a point of this space is a multi-dimensional vector with a one-to-one correspondence to a metamaterial unit cell. These points were then manipulated by evolutionary algorithms, of our design, to find generate unit cells that best exhibit some desired EM response.

In each project we present our findings and discuss the next steps needed to continue this research.

## Chapter 2 : METAMATERIAL GEOMETRY ANALYSIS (University of Texas at Austin)

An important step in the structural design of metamaterials is establishing the relationship between the metamaterial geometry and its constitutive material parameters,  $\mu$ ,  $\epsilon$ ,  $\beta$ , and  $\alpha$ . Here we are concerned with the structural design of periodic metamaterials, in which the entire structure is composed of the repetition of a unit cell. This unit cell is typically composed of a cube with some sort of inclusion at its center. The choice of inclusion, together with the dimensions of the structure and the material used in the space around the inclusion fully determine the bulk material response for an impinging electromagnetic wave.

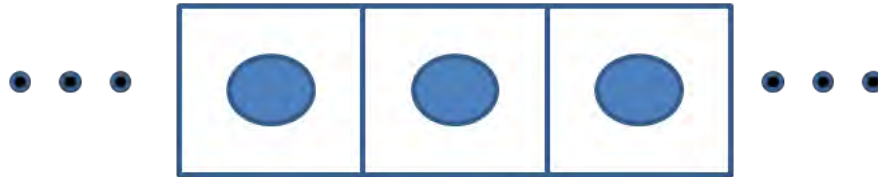


Figure 2.1: 1D Metamaterial. Circular inclusions in a square linear chain

For a 1 dimensional case, we may consider the structure to be a linear chain of unit cells arranged one after the other, as in Figure 2.1. The implementation of useful physical structures requires creating this structure in two or three dimensions. Figure 2.2 and Figure 2.3, below, shows examples of 2-dimensional and 3-dimensional

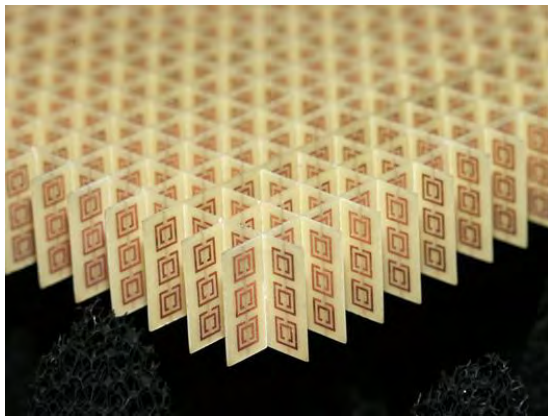


Figure 2.2: 3D Metamaterial. Square split-ring resonators suspended in a lattice[8]



Figure 2.3: 2D Metamaterial. Circular Split ring resonators and wire rods held up on a platform (Smith and Schultz, UCSD)

metamaterial structures. The one on the left is a 3-dimensional metamaterial composed of a cubic lattice (the supporting plastic grid), semi-infinite in  $x, y$ , and of finite thickness in  $z$ . Its inclusions are dual square split-ring-resonators (SRR). On the right we see a similar two dimensional metamaterial, semi-infinite in  $x$  and  $y$ , whose inclusions are composed of dual, circular, SRRs and wire rods.

An important tool in the structural analysis of these metamaterials is the numerical simulation of electromagnetic fields inside them. These are useful in determining the bulk material response as well as the constitutive parameters. In fact, the analytical solution of Maxwell's equations in most scenarios is

not possible. Researchers turn to computational methods to numerically extract the electromagnetic fields in these cases.

In particular, we can solve Maxwell's equations for  $\mathbf{E}$  and  $\mathbf{H}$  in source free conditions, where we consider our point of excitation to be infinitely far away, eliminating the source terms of Maxwell:

2.1

$$\nabla \times \mathbf{E} = -j\omega\mu\mathbf{H}$$

$$\nabla \times \mathbf{H} = j\omega\epsilon\mathbf{E}$$

$$\nabla \cdot \mathbf{D} = 0$$

$$\nabla \cdot \mathbf{B} = 0$$

The resulting solutions are known as *eigenmodal solutions* – self-sustaining solutions to Maxwell that do

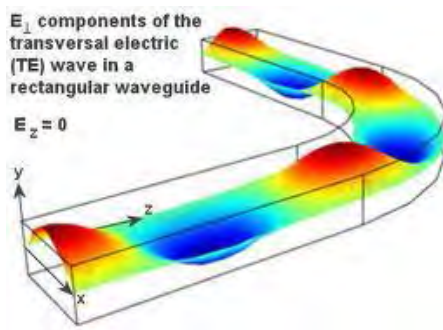


Figure 2.4: Eigenmodal propagation in a rectangular waveguide (<http://universe-review.ca/R13-11-QuantumComputing.htm>)

not require an excitation source. To develop some intuition on this notion, consider a waveguide such as the one shown here, Figure 2.4. The excitement of electromagnetic fields by a Dirac-delta function at one end of the waveguide will propagate through the waveguide to the other end. The distribution of these fields will be a function of the waveguide geometry and they will continue to propagate despite the absence of generative sources. We consider this to be an eigenmodal solution, and the solutions of interest for a periodic metamaterial are analogous.

For the metamaterials of interest here, instead of considering excitation by a point source at one edge, we consider uniform excitation by a plane wave. Note that this

is analogous to placing an oscillating point source infinitely far away – the electromagnetic fields generated by the source will take the form of plane waves as they travel further and further from the source. The eigenmodal solutions to the resultant problem represent the electromagnetic fields distributions within each unit cell (identical for all cells except those close to the boundary).

Of further interest to metamaterial structural design is understanding the way plane waves propagate inside the material structure. As mentioned above, there exist homogenization theories which lend themselves to analytical descriptions of plane wave propagation inside bulk materials based on effective constitutive parameters. These are particularly useful in structural analysis, and much of the work being done in numerical simulations is in the verification of these theories.

In particular, our group is interested in understanding the propagating modes (distinct wavenumbers  $\beta$ ) that can exist in various structures for an impinging electromagnetic wave at frequency  $\omega$ . Using COMSOL, we construct a geometry and solve an eigenvalue problem based on frequency in order to determine these propagating modes. We extend this COMSOL functionality to MATLAB. By turning our COMSOL program into a MATLAB script, we create MATLAB drivers which can sweep frequency over a range of interest to generate dispersion diagrams for a geometry. A dispersion diagram is a plot of  $\omega$  vs.

$\beta$  and determines the relationship between the impinging free space wavenumber  $k_0 = \omega\sqrt{\epsilon\mu}$  and the propagating modes within the structure. The following sections explain why this is of interest in metamaterial design.

## A. Development of COMSOL/MATLAB Interface for periodic full-wave simulation

The development of a computational platform which allows researchers to extract the effective bulk material parameters from a periodic array begins with the verification of a well-known two-dimensional dielectric cylinder problem. We verify that our platform can extract the proper relationship between the impinging free-space wave and the propagating wave in the material. We compare normal incidence to oblique incidence and discuss the differences. The problem begins with the derivation of the equations to solve inside the domain of interest, and continues with running iterative simulations in this domain.

### Weak Form Formulation

We turn to the definition of our problem. The finite element method (FEM) is a computational method for approximating the solutions of partial differential equations (PDE) and integral equations. A solution can be formulated for two and three dimensional problems [9], and we present here, for explanation, the solution formulation for an impinging wave in the  $\mathbf{x}$  direction. That is, normal on the surface of the square with no component in  $\mathbf{y}$ .

We begin by rearranging the first two of Maxwell's source-free equations into the Helmholtz equation in the form:

$$2.2 \quad \nabla \times \left( \frac{1}{\epsilon} \nabla \times \mathbf{H} \right) - \mu \frac{\omega^2}{c^2} \mathbf{H} = 0$$

In general,  $\epsilon = \underline{\underline{\epsilon}}(\mathbf{x})$  and  $\mu = \underline{\underline{\mu}}(\mathbf{x})$  are complex valued, spatially dispersive tensors. In our setup, we take them both to be real-valued constants, and set them to be different within the different subdomains (dielectric cylinder, surrounding free-space).

We will solve for the magnetic field  $\mathbf{H}$  everywhere inside our domain. Bloch's Theorem [10] tells us that we can represent the vector function  $\mathbf{H}$  as a product between a complex exponential propagation term and a spatial, periodic function:

$$2.3 \quad \mathbf{H}(\mathbf{x}) = \mathbf{u}(\mathbf{x}) e^{-j(\omega t - \mathbf{k} \cdot \mathbf{x})}$$

Inserting 2.3 into

2.2 we obtain our field expression (aka equation of motion),

$$2.4 \quad \frac{k_0^2}{\varepsilon_r} \mathbf{u} - \frac{\mathbf{k}}{\varepsilon_r} (\mathbf{k} \cdot \mathbf{u}) - j \mathbf{k} \times \left( \frac{1}{\varepsilon_r} \nabla \times \mathbf{u} \right) - j \nabla \times \left( \frac{1}{\varepsilon_r} \mathbf{k} \times \mathbf{u} \right) + \nabla \times \left( \frac{1}{\varepsilon_r} \nabla \times \mathbf{u} \right) - \mu_r \frac{\omega^2}{c^2} \mathbf{u} = 0$$

Where  $k_0^2 = \omega \sqrt{\mu_0 \varepsilon_0}$  is the free space wavenumber,  $\varepsilon_r = \varepsilon_0 / \varepsilon$  is the relative permittivity, and  $\mu_r = \mu_0 / \mu$  is the relative permeability. This can be considered an eigenvalue problem and be solved for the wavenumber  $\mathbf{k}$ .

COMSOL allows us to specify the field expression to be solved using its FEM solver. This involves setting the integral of the FEM *weak expression* to zero and solving for  $\mathbf{u}$ . We multiply 2.4 by the test function  $\mathbf{v}(\mathbf{x})$  to obtain the weak expression of:

$$2.5 \quad \frac{k_0^2}{\varepsilon_r} \mathbf{v} \cdot \mathbf{u} - \frac{\mathbf{v} \cdot \mathbf{k}}{\varepsilon_r} (\mathbf{k} \cdot \mathbf{u}) - j \mathbf{v} \cdot \left[ \mathbf{k} \times \left( \frac{1}{\varepsilon_r} \nabla \times \mathbf{u} \right) \right] - j \mathbf{v} \cdot \nabla \times \left( \frac{1}{\varepsilon_r} \mathbf{k} \times \mathbf{u} \right) + \mathbf{v} \cdot \nabla \times \left( \frac{1}{\varepsilon_r} \nabla \times \mathbf{u} \right) - \mu_r \frac{\omega^2}{c^2} \mathbf{v} \cdot \mathbf{u} = 0$$

Integrating by parts and setting equal to zero yields two integrals, one over the domain  $\Omega$  of the unit cell, the other over its boundary  $\partial\Omega$ ,

$$2.6 \quad \int_{\Omega} \left[ \frac{k_0^2}{\varepsilon_r} \mathbf{v} \cdot \mathbf{u} - \frac{\mathbf{v} \cdot \mathbf{k}}{\varepsilon_r} (\mathbf{k} \cdot \mathbf{u}) - j \mathbf{v} \cdot \left[ \mathbf{k} \times \left( \frac{1}{\varepsilon_r} \nabla \times \mathbf{u} \right) \right] - j \mathbf{v} \cdot \nabla \times \left( \frac{1}{\varepsilon_r} \mathbf{k} \times \mathbf{u} \right) + \mathbf{v} \cdot \nabla \times \left( \frac{1}{\varepsilon_r} \nabla \times \mathbf{u} \right) - \mu_r \frac{\omega^2}{c^2} \mathbf{v} \cdot \mathbf{u} \right] \cdot d^3x + \oint_{\partial\Omega} dA \cdot \mathbf{v} \cdot \left[ \mathbf{n} \times \frac{1}{\varepsilon_r} (-j \mathbf{k} \times \mathbf{u} + \nabla \times \mathbf{u}) \right] = 0$$

where  $\mathbf{n}$  is the vector normal to the boundary. The natural boundary condition [11] enforces the boundary integral of 2.6 to be zero by forcing  $(-j \mathbf{k} \times \mathbf{u} + \nabla \times \mathbf{u}) / \varepsilon_r$  to be identically zero tangent to the boundary. By noting that we can obtain the electric field from the Bloch-form magnetic field as

$$2.7 \quad \mathbf{E}(\mathbf{x}) = \frac{1}{j \varepsilon_r k_0} \nabla \times \mathbf{H} = \frac{1}{j \varepsilon_r k_0} (-j \mathbf{k} \times \mathbf{u} + \nabla \times \mathbf{u}) e^{-j(\omega t - \mathbf{k} \cdot \mathbf{x})}$$

We see that forcing the boundary to zero is enforcing the perfect electric conductor (PEC) boundary condition  $\mathbf{n} \times \mathbf{E} = 0$ . The effect is to force the tangential electric field component along the boundary to be identically zero.

## 2D Eigenvalue Problem – Normal Incidence

We begin our analysis of metamaterial structures with recreating a two-dimensional scenario.

We design a unit cell by taking an empty (free space) square and inserting a dielectric cylinder into it. For realism we treat this as a three dimensional problem constrained to two dimensions. That is, everything is uniform along the  $z$  direction.

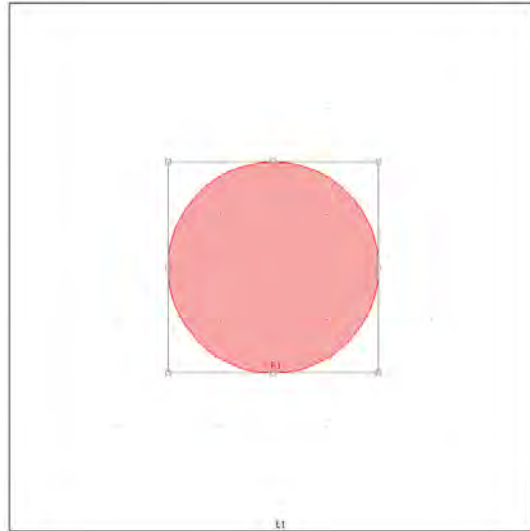
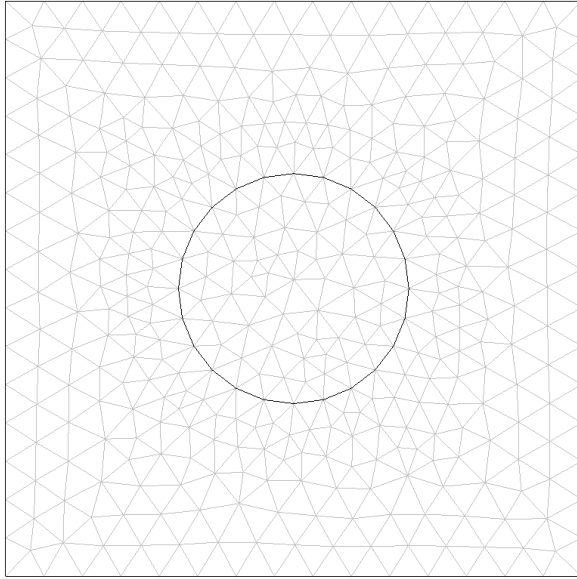


**Figure 2.5: 2D Eigenvalue Problem Geometry. Dielectric Cylinder with  $\epsilon_r=10$ ,  $\mu_r=1$ , radius  $a = 0.2$  cm, side length  $d = 1$  cm**

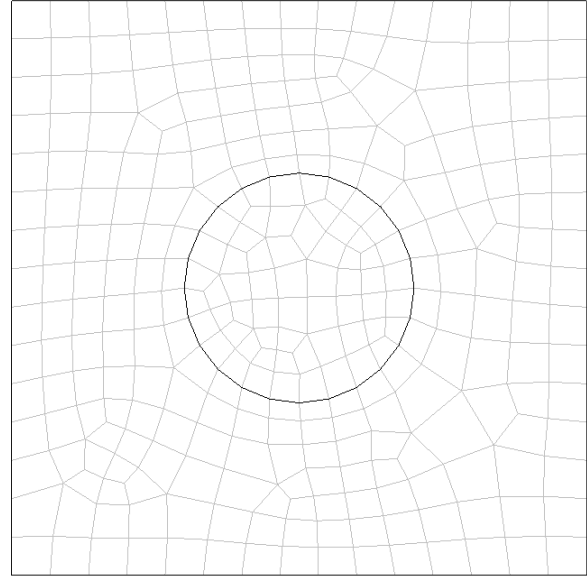
We set  $\epsilon_r=10$  and  $\mu_r=1$  inside the cylinder. We are seeking a purely electric response with no magnetic response. Setting  $\epsilon_r=10$  ensures a strong electric response and setting  $\mu_r=1$  maintains  $\mu = \mu_0$ .

It is common in the design of metamaterials to make the inclusions very dense in the lattice. For this geometry that would require the radius of our sphere to approach half the square's sidelength. However, in this particular case, we would like to analyze a less tightly-packed metamaterial. We thus set the cylinder's radius to  $a = 0.2$ cm for a normalized unit cell length of  $d = 1$ cm. Recall that this is an analysis of just one cell, but the material itself is a periodic repetition of it.

We continue the setup of this problem with mesh generation. COMSOL, for 2D problems, offers a tetrahedral and quadratic meshing scheme, in which the region of interest is populated with tetrahedrons, or squares, respectively.



*Tetrahedral Mesh*



*Quadratic Mesh*

**Figure 2.6: Tetrahedral and Quadratic Meshing Schemes**

Figure 2.6 shows our two options for meshing schemes. As we can see, COMSOL's meshing algorithm fits the corners of our mesh elements to the boundaries of our subdomains. This is an interesting feature that will be useful if, after extracting an electric field distribution from this problem, we are interested in calculating the magnetic field using  $\nabla \times H = j\omega\epsilon\bar{E}$ . We keep the tetrahedral mesh.

In this scenario, we consider normal incidence in  $\mathbf{x}$ , with  $\mathbf{k} = k_x \mathbf{x}$  and  $\mathbf{u} = u_x \mathbf{x} + u_y \mathbf{y}$ . We combine these with Equation 2.5 and insert them into COMSOL. We force our boundary to be periodic, ensuring PEC conditions, and use an eigenvalue solver to solve for  $\mathbf{k}$  and  $\mathbf{u}$ .

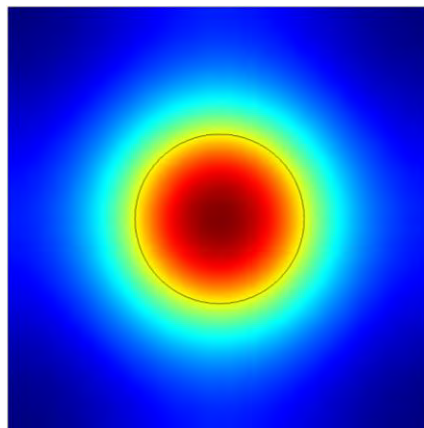
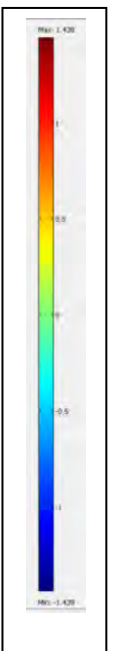


**Figure 2.7: H Field distribution for propagating mode  $f = 0.143$  and  $k = 0.438$**

Figure 2.7 shows the magnetic field distribution for a propagating mode, calculated for frequency  $f = 0.143$ . For the propagating mode  $k = 0.438$  we observe a maxima at the center of our cylinder, and



minima near the boundaries. This frequency corresponds to a wavelength of 20.97 cm, and with the inclusion radius set to  $a=0.2\text{cm}$ , as above, we are in the quasi-static region since  $2a < \lambda/10$ .

We observe from the field distribution that the primary response at this excitation is due to the magnetic dipole moment induced in the dielectric cylinder. Circulating currents in the cylinder produce a magnetic response dominated by this first term of the multipole expansion. This is to be expected given the relative size of the particle. Since the particle is so small compared to the size of the wavelength, higher order terms contribute very little to the overall response.

Effectively, utilizing COMSOL in this fashion allows us to input frequency and extract both wavenumbers and magnetic field distributions that can exist for an impinging wave with frequency  $\omega$ . We can further automate this procedure by linking COMSOL with the popular computational software MATLAB. COMSOL allows a geometry, mesh, accompanying parameter settings, and solver kernel to be saved and called from a MATLAB .m file. We leverage this capability to create a MATLAB function which takes as arguments frequency and the number of eigenvalues desired and returns the propagating wavenumbers  $\mathbf{k}$ .

Sweeping this function over a frequency range allows us to create what is known as a *dispersion diagram* for our metamaterial structure. This plot of frequency versus the real part of the propagating wavenumber is shown below. It provides valuable information about the sort of structure we are dealing with. The diagram below shows only those modes which have very small imaginary components ( $<0.001$ ). Complex valued  $\mathbf{k}$  are not of particular interest to us, since their propagation will decay rapidly in space.

The periodic repetition of the bands dissects the dispersion diagram into its square Brillouin Zones [12]. In fact, although not shown below, these bands are symmetric for  $\text{real}[\mathbf{k}] < 0$ . The vertical lines  $\text{Re}[\mathbf{k}]d = n\pi$  for all integer  $n$  are lines of symmetry of this space. This is due to the representation of  $H$  as a product of  $\mathbf{u}$  and a complex exponential. The exponential term will not change if  $kd$  becomes  $(k+2\pi)d$  and it will reverse sign if  $kd$  becomes  $(k+\pi)d$ . In this scenario  $d = 1$  so we observe these symmetry lines at  $\text{real}[\mathbf{k}] = n\pi$ . This thus restricts our interest to the domain  $0 < \text{Re}[\mathbf{k}]d < \pi$ .

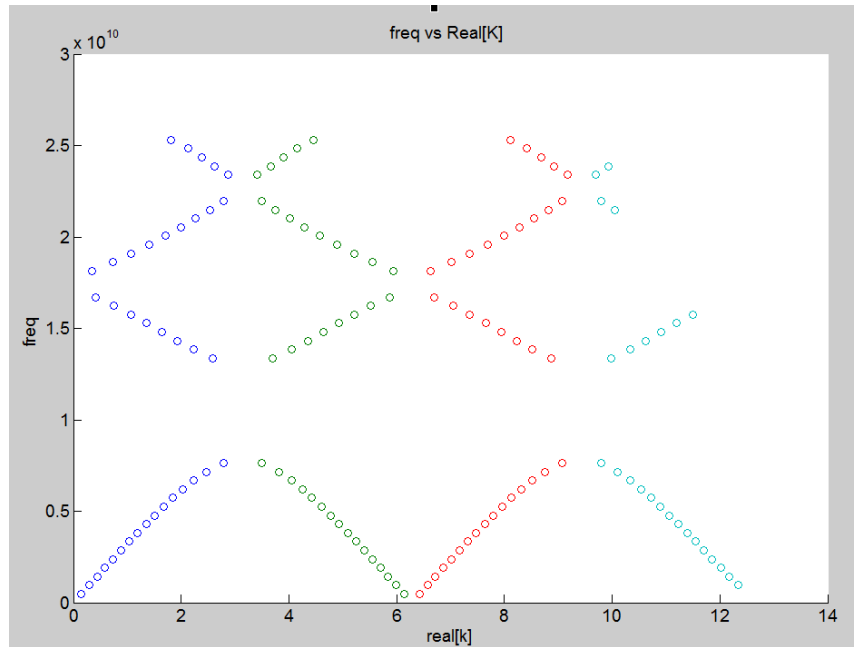


**Figure 2.8: Dispersion diagram for wave propagation in the x direction for a 2D metamaterial composed of a dielectric cylinder inside a square unit cell.**

We further note that band gaps exist in which propagation does not occur. In the frequency range  $0.76 < f < 1.33$  the only modes we find are evanescent modes with complex  $k$ . Physically this means that within these frequency ranges the scattering off of the dielectric cylinder is so great that it prevents the propagation of any mode. As the frequency increases to this cutoff, the wavelength decreases until it is sufficiently small to cause resonant H-field perturbations in the unit cell. This renders propagation impossible until the frequency crosses the next cutoff in one of the upper bands. Note, however, that at this frequency ( $f=1.337$ ) the wavelength is reduced to 2.24cm, and so our inclusions are now comparable to the size of the wavelength, and we are no longer in the quasistatic limit.

With these two considerations in mind, we now restrict our interest to the first Brillouin zone. This restricts our analysis to the frequency range  $0 < f < 1.7$  and wavenumber range  $0 < \text{Re}[k]d < \pi$

We have seen the H field distribution for a low frequency. We now consider frequencies near the lower and upper cutoffs, and near the high end of the Brillouin zone. Figure 2.9 below shows the magnetic field distribution near the top of the first band, approaching the cutoff, at a frequency of 0.764 with a wavenumber of 2.78. As before, we see the maximum occur in the dielectric center, with minima along the left and right edges. In contrast with Figure 2.7, the zero region (colored green) extends to the top and bottom of the cell. Keeping in mind the periodicity of the metamaterial, this means that propagation through such a material will look like a series of troughs (blue) interrupted by singular peaks (red).

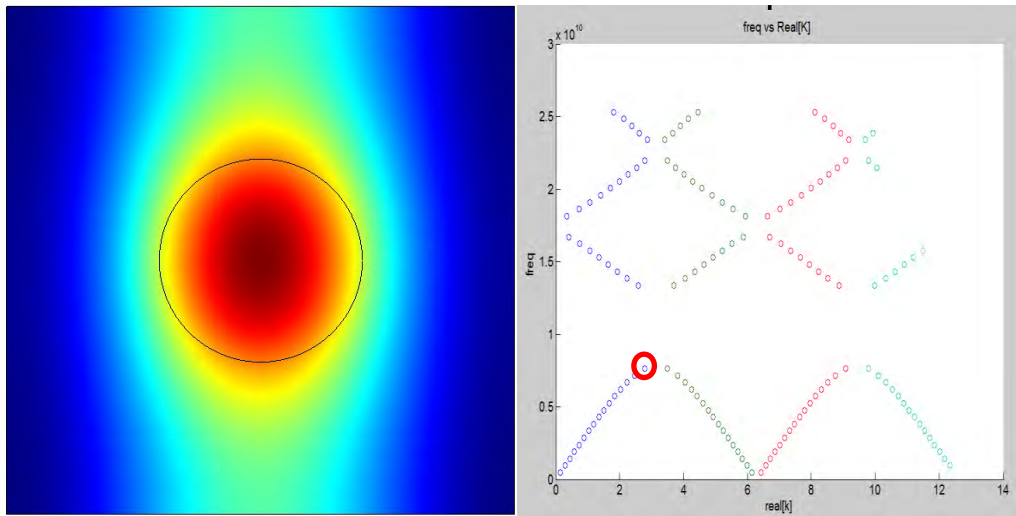


Figure 2.9: H field distribution near the first cutoff  $f = 0.764$  and  $k=2.78$

So what happens in the bandgap? As stated above, the band gap resonances prevent propagation. Nevertheless, there still exist evanescent modes. Figure 2.10, below, shows the magnetic field distribution for a wave at frequency  $f = 1.1$  with wavenumber  $k = \pi + i0.9$

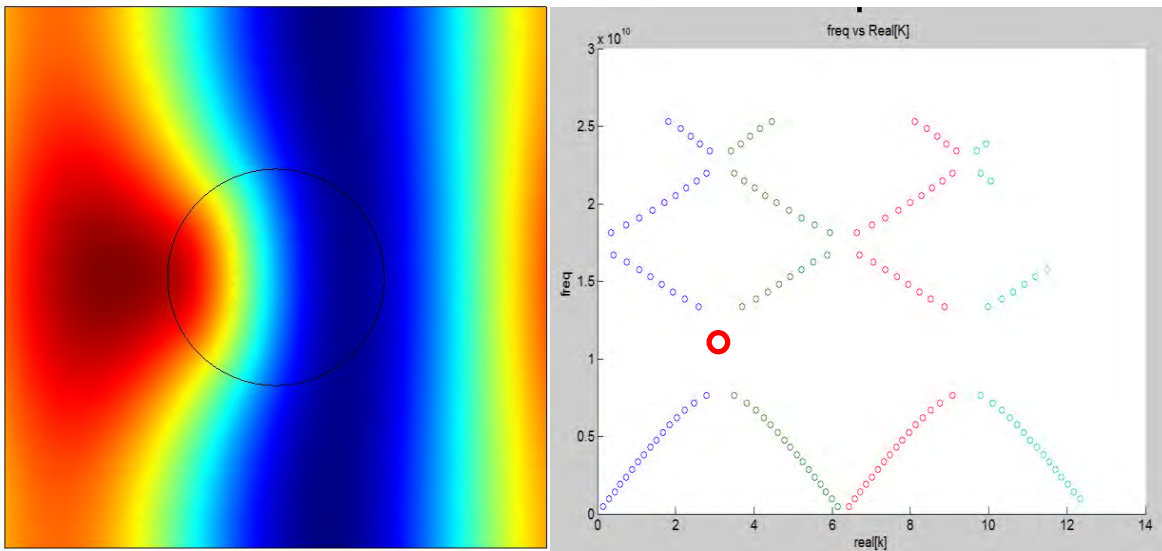
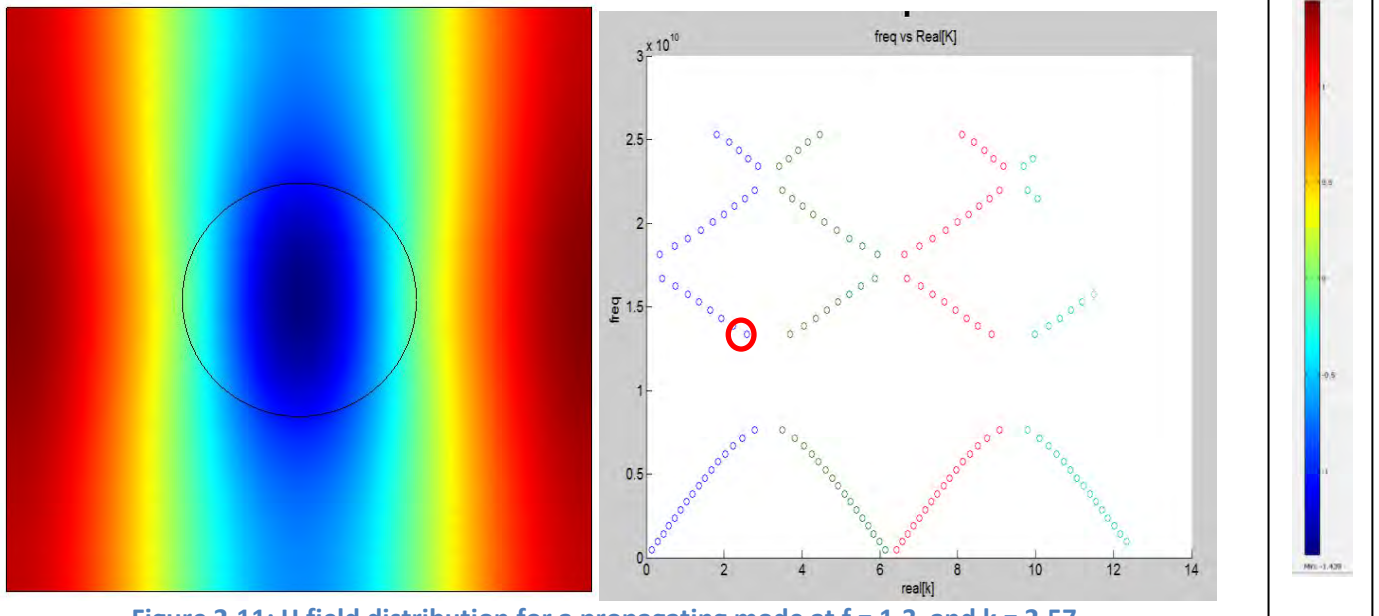


Figure 2.10: Evanescent Mode in band gap at  $f = 1.1$ ,  $k = \pi + i0.9i$

It is characteristic of many evanescent modes in this problem to exhibit an asymmetry along the axis perpendicular to propagation. We observe here a maximum that occurs prior to the wave striking the dielectric cylinder, as the wave's crest bulges into the material.

Next, we observe the magnetic field immediately above cutoff, at frequency  $f = 1.3$  and wavenumber  $k = 2.57$ . Figure 2.11, below, shows this distribution.



**Figure 2.11: H field distribution for a propagating mode at  $f = 1.3$  and  $k = 2.57$**

Immediately we see a similarity to Figure 2.9, the H field for the propagating mode right before the band gap. Both field distributions follow a pattern of vertical striations. We see it more pronounced for this distribution above the band gap, yet the mode below it shares this property as well.

Finally, we turn our attention to the magnetic field distribution at the highest frequency within the first Brillouin zone. Figure 2.12, below, shows this. Unsurprisingly, we see a field distribution similar to that of Figure 2.7, albeit inverted, with a crest along the boundary and a trough in the dielectric interior. Even though the exterior free-space excitation waves are at different frequencies, the propagating wavenumber is almost the same for both cases. As a result, the wave in the material propagates with the same periodicity in both cases, and thus, similar magnetic field distributions.

This is analogous to the similarities between Figure 2.11 and Figure 2.9. In this case we again note that both modes propagate with similar wavenumbers, yet at different frequencies. Their differences in magnetic field distributions are a result of their proximity to the band gap. As a mode approaches the bandgap it threatens to become evanescent. As a result, its field distributions become fairly unpredictable.

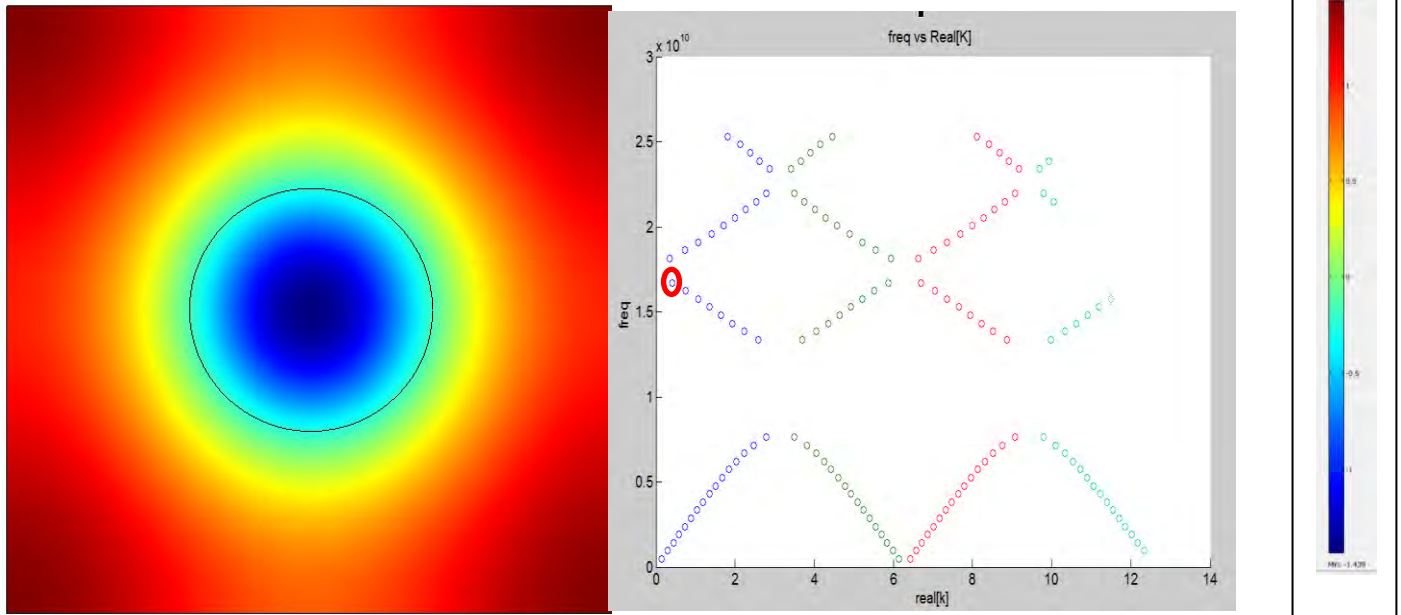


Figure 2.12: H field distribution at the top of the first Brillouin Zone.  $f = 1.67$ ,  $k = 0.42$

### 2D Eigenvalue Problem – Oblique Incidence

We now briefly turn our attention to oblique incidence of this structure and discuss the propagating radiation that results within our dielectric sphere arrangement

Instead of impinging radiation normal to the unit cell boundary, we now impinge it at a  $30^\circ$  angle to the boundary normal. Figure 2.13, below, shows the normalized dispersion diagram for this angle of incidence in the first Brillouin zone.

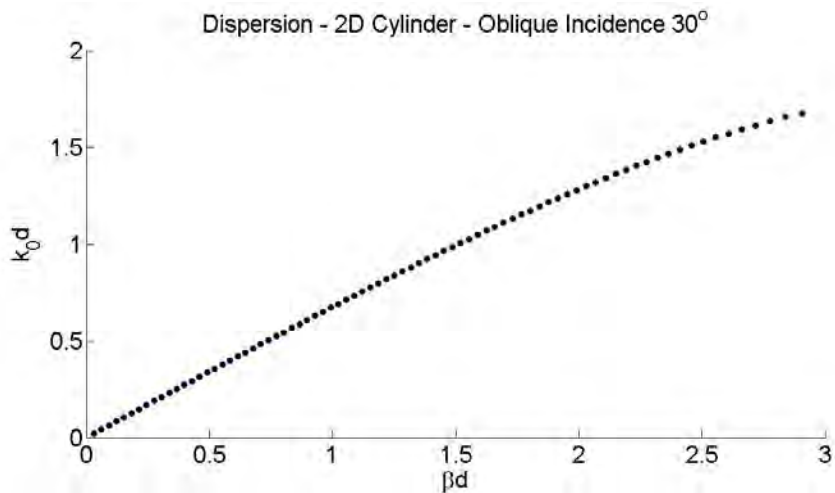


Figure 2.13: 2D Dielectric Cylinder Oblique Incidence  $30^\circ$

Immediately we notice a similar pattern to that of normal incidence (a bell shaped curve), but we notice that the y-axis has shifted. We see first-zone propagation for higher  $k_0d$  and thus higher frequency. This results from the angle shift. The wave no longer ‘sees’ a series of unit cell cubes separated by a center-to-center distance of  $d = 1\text{cm}$ , but instead, a different arrangement which depends on this angle of incidence. The resulting periodicity shifts the dispersion diagram.

This is made clearer in Figure 2.14, below. Here we show oblique incidence at  $60^\circ$  instead of  $30^\circ$  over four adjacent Brillouin zones. Due to the symmetry of the problem, we are not surprised to see that the first Brillouin zone exactly matches that of the  $30^\circ$  incidence case. What is interesting, however, is the fact that the apex of the lower curve has shifted to the right. Under normal incidence we expect  $\beta d = \pi$  to be the apex point. Since we are impinging obliquely now, the wave’s possible phase shift within the cell extends to  $\pi/\cos(\theta)$ .

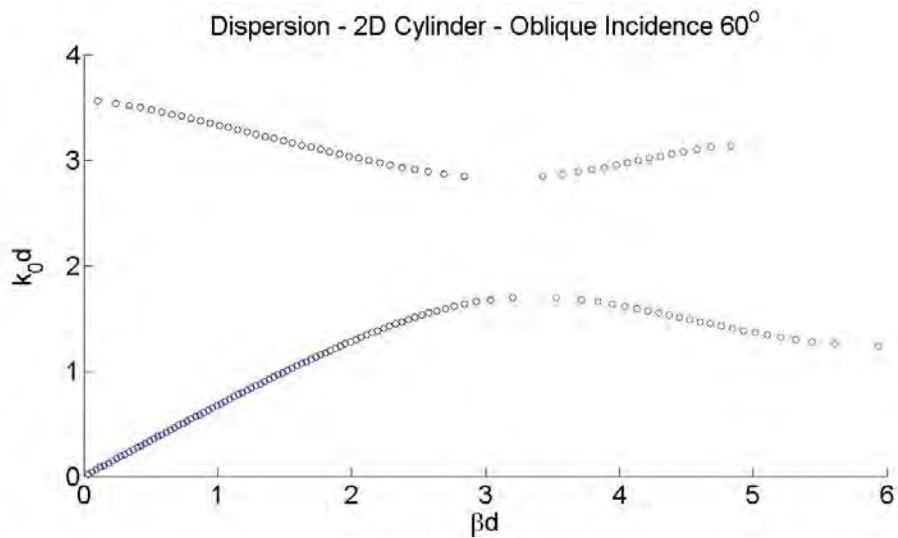


Figure 2.14: 2D Cylinder - Oblique Incidence at  $60^\circ$

This analysis for normal and oblique incidence verifies our platform’s 2D functionality.

## B. Dielectric Sphere

We move onto its verification in three dimensions. This poses a much more challenging problem to formulate. We must now consider the impingement of the wave in vector form, as below:

$$2.8 \quad \mathbf{k} = \beta \begin{pmatrix} kxn \\ kyn \\ kzn \end{pmatrix}$$

$$1 = kxn^2 + kyn^2 + kzn^2$$

Where  $kxn$ ,  $kyn$ , and  $kzn$  form a unit vector satisfying the relation above, and  $\beta$  represents the propagating mode’s wavenumber.

This is of interest to us because it allows us to extend our model to three dimensions. The magnetodielectric sphere is a well-studied problem with known dispersion curves. By recreating it here with COMSOL, we can verify the resultant curves against those of, say, CST Microwave Suite, and ensure our platform's functionality.

### COMSOL/MATLAB Formulation

By setting up a 3D eigenvalue problem for a dielectric sphere [13], we create a COMSOL model of a dielectric sphere with  $\epsilon_r = 10$ ,  $0.2d=r$ , where  $d$  is the unit cell side length,  $r$  is the radius, and  $\epsilon_r$  is still the relative permittivity.

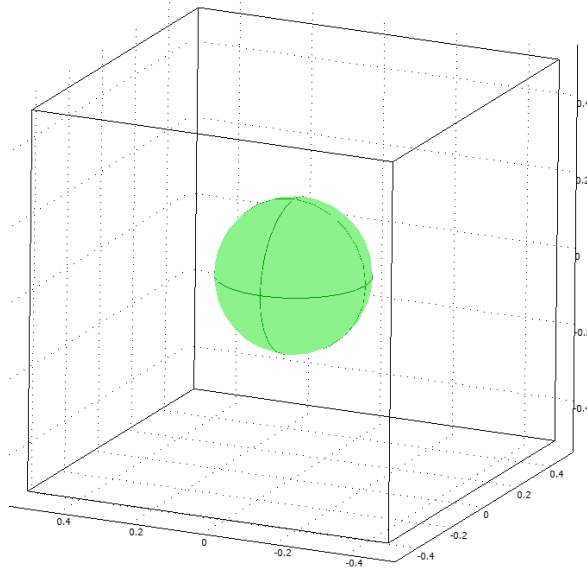


Figure 2.15: Dielectric Sphere

This is not a particularly dense configuration with a  $0.6d$  separation distance from one edge of the sphere to the adjacent cell's sphere in the periodic lattice. We expect low coupling between adjacent cells and a dispersion curve similar to those shown for the two-dimensional cases.

### Dispersion Analysis

Shown below in Figure 2.16 are the resultant dispersion curves of this structure generated by COMSOL. We observe that, unlike the curves for the two dimensional case, here we have a very small band gap. Propagation exists almost contiguously between the first and second Brillouin zones. Of course, there must always be some sort of gap for such a structure. At a certain frequency the mie scattering resonances [14] will be strong enough to prevent any propagating wave from getting through, opening a frequency gap in the dispersion curve. What's interested about this structure is that the lower band closely follows the dispersion of free space. It is not apparent from the chart below, but a frequency of  $1.5 \times 10^{10}$  Hz corresponds to  $k_0d = 2\pi f/c*d = \pi$ . Since this happens at  $\beta d = \pi$  and the lower curve is almost linear, the dispersion in the first Brillouin zone closely follows that of free space.

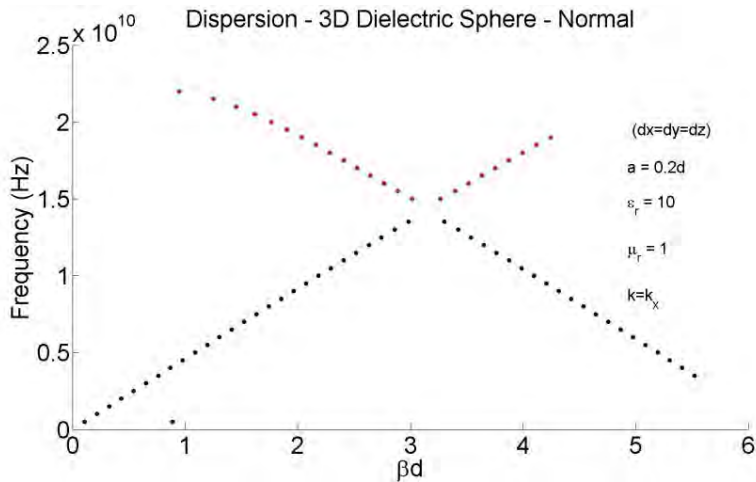


Figure 2.16: 3D Dielectric Sphere Dispersion Curves – COMSOL

Upon first glance it may appear that the dispersion curve is incorrect. After all, we expect some sort of response from the dielectric sphere even at lower frequencies. However, further dispersion calculation with CST Microwave Suite confirms our findings.

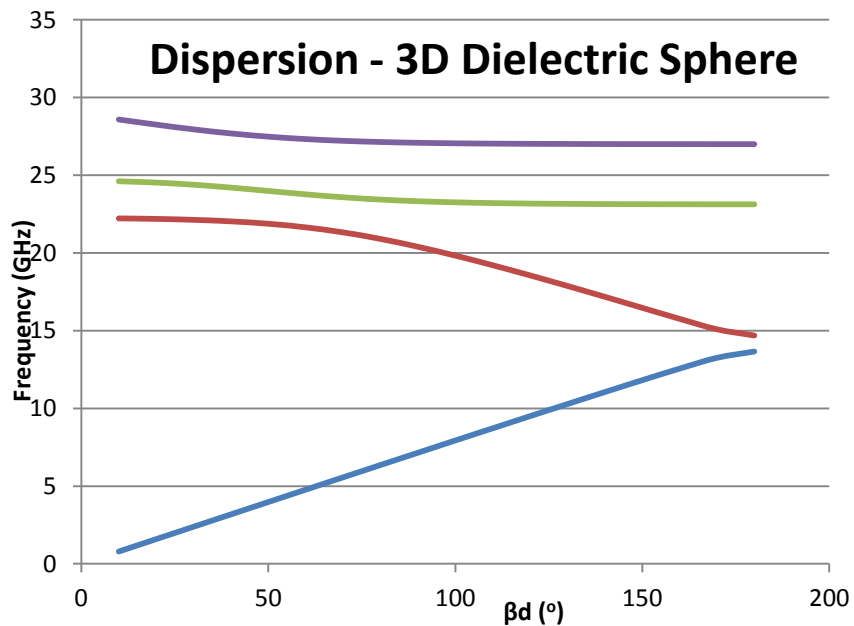


Figure 2.17: 3D Dielectric Sphere Dispersion Curves - CST

This implies that at these long wavelengths the sphere is not large enough nor does it have a permittivity sufficiently strong to elicit much of a response from the impinging wave. The propagating wave effectively sees close to no medium. The matching of these curves confirms the ability of our COMSOL method to calculate accurate dispersion curves for normal incidence.

We omit the verification of oblique incidence dispersion. It is of no further interest to our discussion. The following scenarios consider only normal incidence.

## C. Plasmonic Spheres

We now turn our attention to new metamaterial geometries. With our computational analysis platform verified, we start analyzing a different type of unit cell inclusion, plasmonic spheres, with the intention of developing optical frequency metamaterials

There are many challenges in optical frequency metamaterials. Since metamaterials typically require quasi-static excitation and the largest visible light wavelength is 750nm, the dimensions of a metamaterial unit cell in the optical region are required to be on the order of tens of nm. In turn this creates a myriad of issues in manufacturing of optical metamaterials. Not only are engineers required to use expensive nano-fabrication techniques, there are many limitations to being able to construct an accurate geometry. Creating an ultra-small suspension lattice is a challenge, and any geometry with very fine details (such as split ring resonators) are considerably more difficult to manufacture.

Furthermore, material properties begin to change. As mentioned in preceding sections, metals shift from good conductors to plasmonic materials with permittivity

$$2.9 \quad \varepsilon(\omega) = \varepsilon_0 \left( 1 - 3 \left( \frac{\omega_p}{\omega} \right)^2 \right)$$

Due to the negative dispersion of this curve at lower frequencies, we thus hypothesize that we can make a metamaterial out of plasmonic particle inclusions. This serves several purposes. Initially, it simplifies the metamaterial's fabrication. It is much easier to make spherical nanoparticles than complicated geometries such as SRRs. Furthermore, the isotropy of a sphere encourages the question, can we make an isotropic metamaterial at optical frequencies?

We consider henceforth three different arrangements of plasmonic spheres, following a theoretical paper suggesting that they can be used for backward-wave propagation [15]. We consider three cases:

- 1) Isotropic metamaterial, in which we center a plasmonic sphere inside a cube
- 2) Linear Chain metamaterial, in which plasmonic spheres create long chains
- 3) Planar Array metamaterial, in which plasmonic spheres form planes

For the following three cases we restrict the simulations to normal incidence along the x direction for the impinging plane waves.

### Isotropic Case

We begin with a unit cell representing a densely packed metamaterial lattice. We center a plasmonic sphere following the dispersion of 2.9 in a unit cube as below

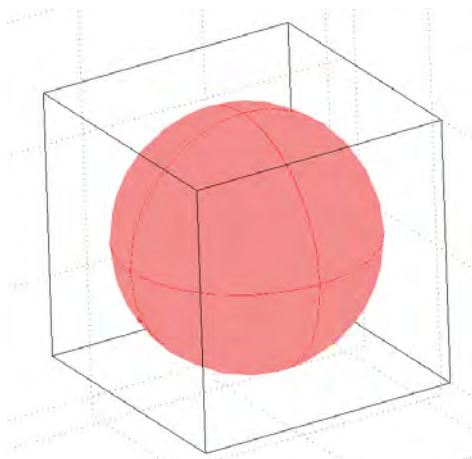


Figure 2.18: Isotropic Sphere

$$\omega_p = 1.979 \times 10^{10}$$

$$2.1a = d$$

$$dx = dy = dz$$

$$\varepsilon = \varepsilon_0 \left( 1 - 3 \left( \frac{\omega_p}{\omega} \right)^2 \right)$$

Where  $a$  is the sphere's radius,  $d$  is the cube's side length, and  $dx$ ,  $dy$ ,  $dz$  are the side lengths of the  $x$ ,  $y$ , and  $z$  sides, respectively.

This type of metamaterial would be the easiest to manufacture. A periodic arrangement of such nanospheres can easily be mimicked by say, a suspension of such spheres in a hydrogel or other such substance with little to no optical EM response.

Figure 2.19 shows the dispersion in the first Brillouin zone for a normally incident plane wave. We see immediately that our hypothesis does not apply well to this geometry at this plasma frequency. The curve follows the shape of a magnetodielectric sphere, and does not exhibit the negative slope needed for a backward wave. It does, however, hint at the possibility of negative group velocity ( $\frac{\partial \omega}{\partial \beta} < 0$ ) if we

were to arrange the spheres differently. We notice that this curve begins to taper off fairly quickly, around  $\beta d = 2$ , and stays flat as  $\beta d$  increased to its apex at  $\pi$ .

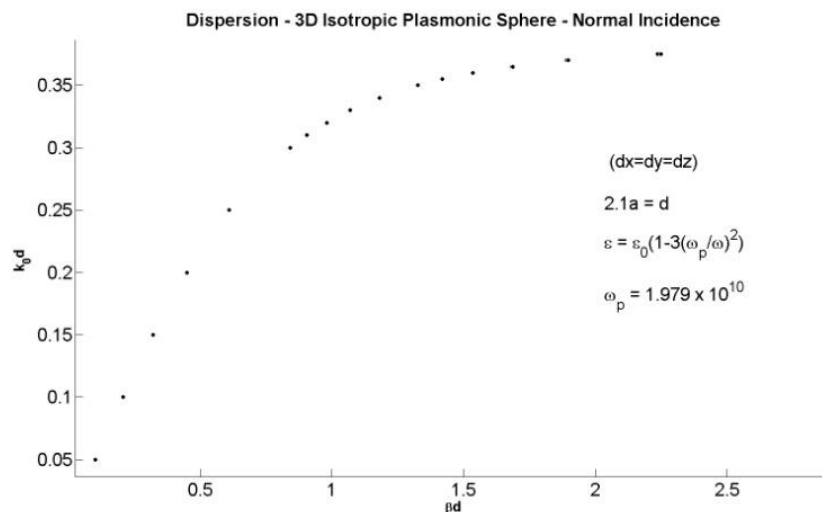
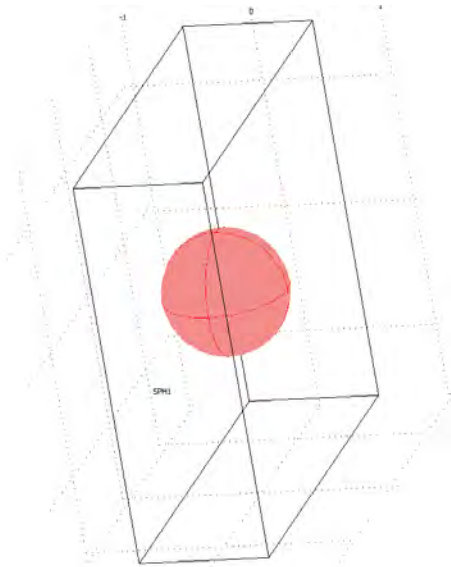


Figure 2.19: Isotropic Plasmonic Sphere Dispersion

Perhaps in a different arrangement we can force the tail of this curve down and shift the apex to the left. Doing so would introduce a band of negative slope, backward wave propagation, and thus a viable metamaterial.

### Linear Chain Case

The next arrangement to attempt is that of a linear chain. We center a Drude model plasmonic sphere inside a rectangular box as below,



**Figure 2.20: Linear Chain Plasmonic Sphere Arrangement**

$$\begin{aligned}\omega_p &= 1.979 \times 10^{10} \\ 2.1a &= d \\ 3dx &= dy = dz \\ \epsilon &= \epsilon_0 \left( 1 - 3 \left( \frac{\omega_p}{\omega} \right)^2 \right)\end{aligned}$$

With  $3dx=dy=dz$ . Envisioning an infinite periodic array of such inclusions we see that they will form chains of nanospheres with center-to-center separation distance of  $dx$  along the chains. Each chain will be separated from its four nearest neighbors by  $3dx = dy = dz$  and by  $3\sqrt{2}dx = dy = dz$  from its four other neighbors.

This is of interest to us due to the separation distance between chains as well as the separation distance between individual particles in any given chain. We expect the strong coupling between particles in a chain will encourage propagating modes to travel along it.

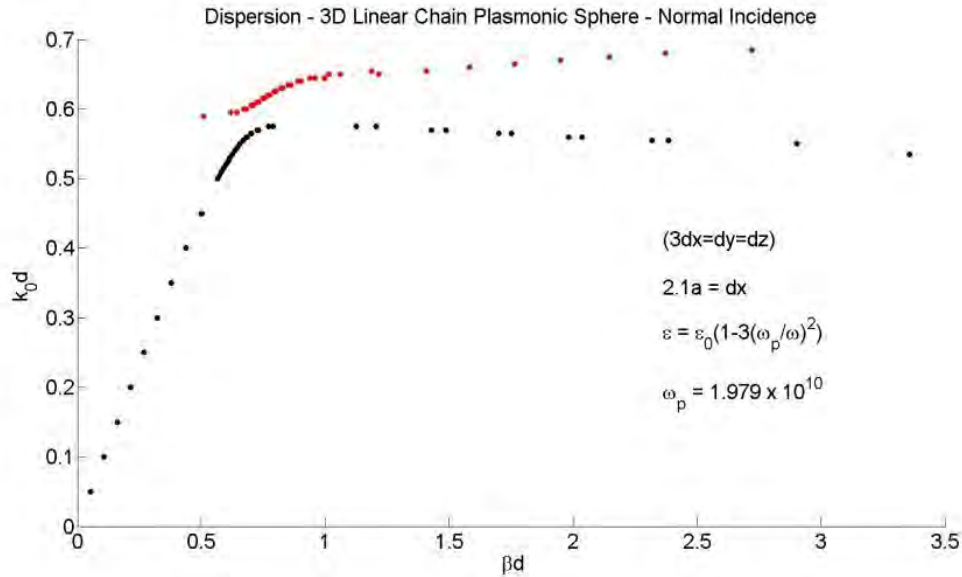


**Figure 2.21: Linear Chain Dispersion**

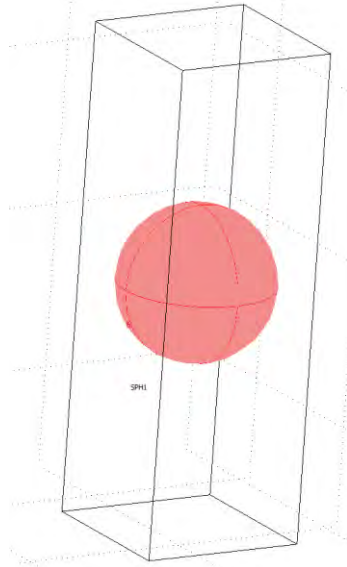
Figure 2.1, above, shows the dispersion curves for the linear chain configuration. Immediately we notice the vast difference between this case and those previously studied. The apex of the first curve occurs at  $\beta d = 0.77$ ,  $k_0 d = 0.58$  as opposed to the dielectric case at  $\beta d = \pi$ . Moreover, we observe backward wave propagation for  $0.535 < k_0 d < 0.575$ , confirming our prior hypothesis. This analysis thus shows that in the same frequency band this structure exhibits both forward and backward wave propagation. This further lends credit to the idea that one mode hugs the linear chains (backward mode), while the other propagates between the chains (forward mode).

Immediately above this first band we observe the second band appearing after a very small bandgap around  $k_0 d = 0.59$ . While it does not exhibit backward-wave propagation, it exemplifies the difference between modes of this material and those of the isotropic and magnetodielectric cases. It is typical to find backward waves at the second band, as was previously shown. Here, however, we see positive slope and thus forward-wave behavior in this second Brillouin zone.

We note that in this same region, there also exists forward-wave propagation at smaller values of  $\beta d$ , and we thus conclude that planar arrays exhibit both forward and backward-wave propagation in the same frequency band. This lends credit to the idea that for a given frequency range, there exists a backward mode hugging the nano-sphere planes and a forward mode that exists in between them.

### Planar Array Case

Our final plasmonic sphere configuration is that of a planar array. We center a Drude model plasmonic nano-sphere inside a parallelepiped, as shown below.



$$\omega_p = 1.979 \times 10^{10}$$

$$2.1a = d$$

$$3dx = 3dy = dz$$

$$\varepsilon = \varepsilon_0 \left( 1 - 3 \left( \frac{\omega_p}{\omega} \right)^2 \right)$$

Figure 2.22: Planar Array Plasmonic Sphere

As for the linear chain case, we envision a periodic array of such unit cells and see that they form planar sheets of nanospheres, each separated from its nearest neighbor by  $dx$ , and each sheet separated from the next by  $3dx=dz$ .

This is of interest to this topic for reasons similar to the linear chain case. It is our hope that the tight coupling between nanospheres in the same sheet will induce propagating modes along the sheets, creating an in-plane isotropy for these modes.

Figure 2.23: Planar Array Dispersion below, shows the dispersion diagram for this configuration. As expected, we see backward-wave propagation in a frequency band immediately adjacent to the apex of the curve at  $\beta d = 0.98$ ,  $k_0 d = 0.579$ . This is in the region  $0.561 < k_0 d < 0.579$ .

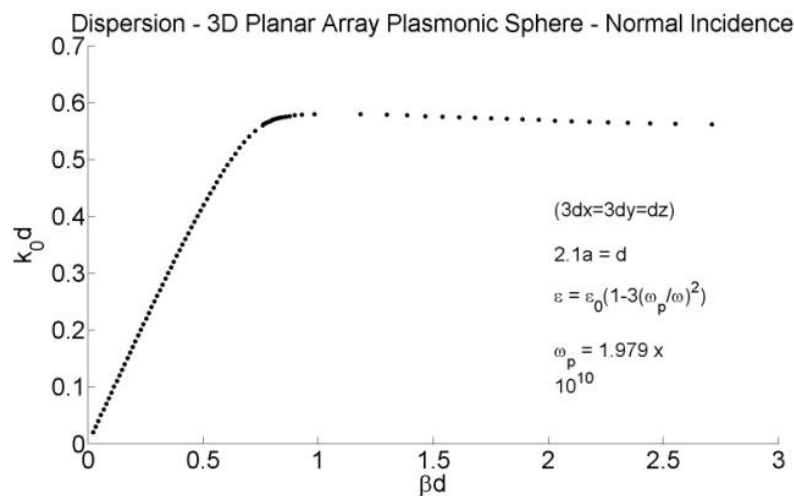


Figure 2.23: Planar Array Dispersion

We note that in this same region, there also exists forward-wave propagation at smaller values of  $\beta d$ , and we thus conclude that planar arrays exhibit both forward and backward-wave propagation in the same frequency band. As in the prior case, this lends credit to the idea that for a given frequency range, there exists a backward mode hugging the nano-sphere planes and a forward mode that exists in between them.

### Arrangement Comparison

In this section we present a comparison between the three cases derived above.

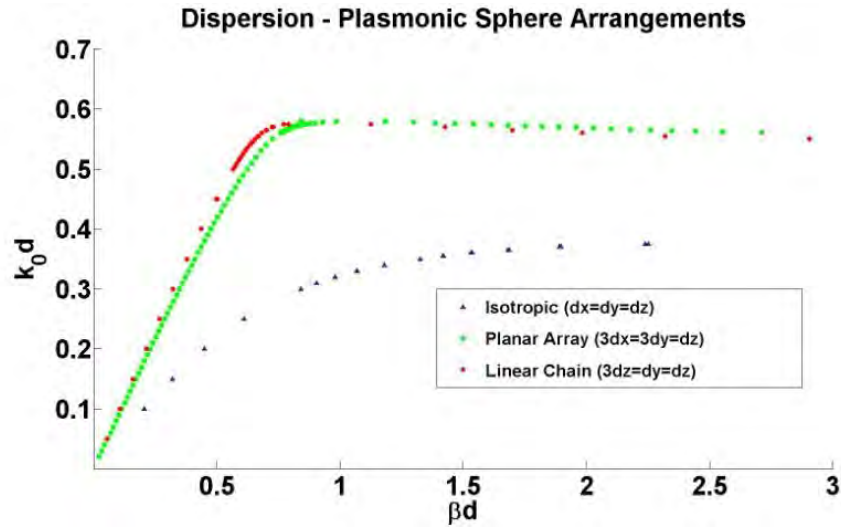
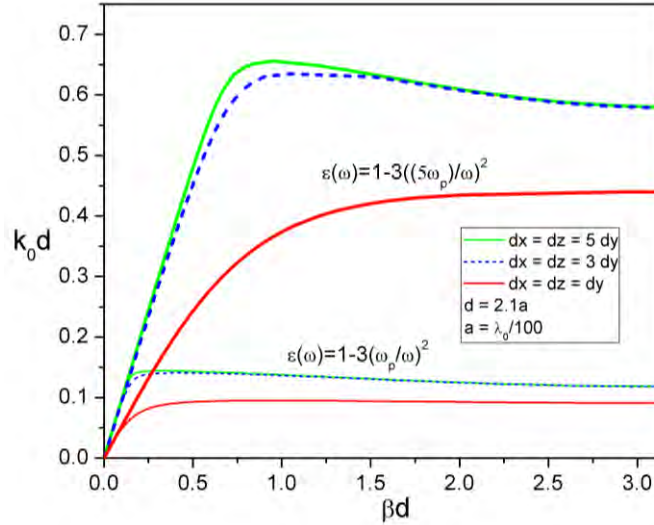


Figure 2.24: Dispersion of Plasmonic Sphere Arrangements

Figure 2.24, above, shows a comparison of the prior three cases. The differences become immediately apparent. The isotropic case's first Brillouin zone is contained in a smaller frequency range than the other two. The isotropic is bounded by  $k_0 d = 0.375$  whereas the other two bands are bounded by  $k_0 d = 0.58$ . Furthermore, as was stated above, the planar array and linear chain both exhibit backward wave propagation in a certain frequency band, whereas the isotropic case does not.

In comparison to the analytical curves shown below in Figure 2.1, we see close proximity between the rigorous computational approach of COMSOL and these approximate curves.



**Figure 2.25: Analytical Results – Dispersion of Plasmonic Sphere Arrangements**

In these analytical results, a dipolar approximation was used for the nanospheres, and the plasma frequency of the upper curves is the same as the plasma frequency used in the COMSOL method. In the analytical case, both the isotropic and the linear chain curve follow the same shape as the COMSOL results. The slight differences in  $k_0 d$  values are attributed to the dipole approximation used.

For emphasis, an additional curve for  $dx=dz=5dy$  was calculated in Figure 2.25. This shows that an increase in the separation distance between the linear chains results in a broader bandwidth backward-wave region. As this case approaches  $\beta d = \pi$  it tapers down to the curve of  $dx=dz=3dy$ . However, its apex at  $\beta d = 0.75$ ,  $k_0 d = 0.66$  is higher than the  $dx=dz=3dy$  apex at  $\beta d = 0.98$ ,  $k_0 d = 0.63$ .

The lower set of curves, for  $\omega_p = \frac{1.979 \times 10^{10}}{5}$  experience backward waves as well, but for smaller bandwidths. What is interesting, however, is that the isotropic case demonstrates backward-wave behavior as well. We expect these lower curves for smaller  $\omega_p$  since this lowers the plasmonic resonance frequency.

Moving forth, we zoom into the backward-wave region of Figure 2.24 for the linear chain and planar array configurations. The curves, shown below in Figure 2.26 highlight the backward-wave region of these structures. As stated above and seen below, the planar array achieves higher frequency values at which backward waves can exist. However, the linear chains exhibit larger bandwidth. The planar array only achieves a bandwidth of  $0.018 k_0 d$  while the linear chain shows a bandwidth of  $0.025 k_0 d$ .

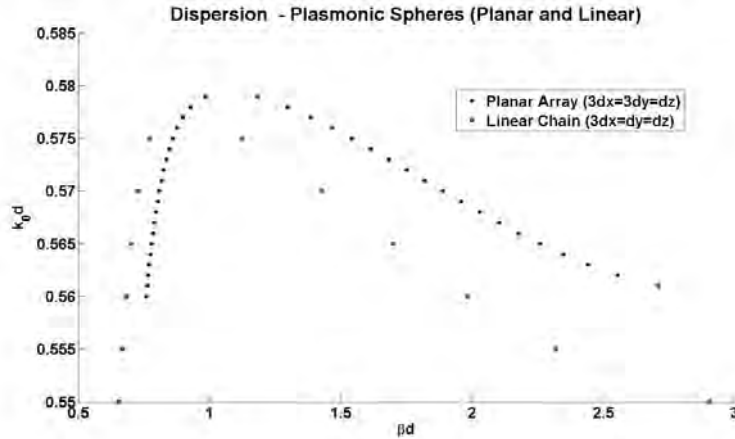


**Figure 2.26: Zoomed-in Dispersion of Planar Array and Linear Chain Arrangements**

We thus conclude that both the planar array and linear chain configurations can support backward-wave propagation while the isotropic case may support this at lower values of the plasma frequency  $\omega_p$ . We further conclude that the linear chains exhibit higher relative bandwidth than the planar arrays.

#### **D. Core-Shell Structure**

Of great importance to optical-frequency metamaterials is being able to establish magnetic responses at these frequencies. Materials such as gold, aluminum, and other metals tend to lose their magnetic responses at these frequencies. As a result, the relative permeability of materials tends to be 1.

This motivates researchers to find ways around this. Discovering a unit cell structure with a strong magnetic and electric response at optical frequencies would open a realm of possible application extensions to the optical frequency spectrum. A conjugate-matched metamaterial superlens with permittivity and permeability opposite to that of free space may become possible in the optical spectrum. This could lead to advanced imaging techniques and other interesting applications.

We thus postulate that a plasmonic-dielectric combination may result in a metamaterial with a magnetic response at optical frequencies. We construct a cubic metamaterial unit cell by placing a small plasmonic sphere at the center of a cube and wrapping a dielectric shell around it. The dielectric shell radius follows the same density as in the preceding plasmonic-sphere scenarios, with  $2.1a = d$ , where  $a$  is the shell radius and  $d$  is the unit cell length. The interior plasmonic sphere's radius is 0.25 that of the shell. The resulting unit cell is shown in Figure 2.27 below.

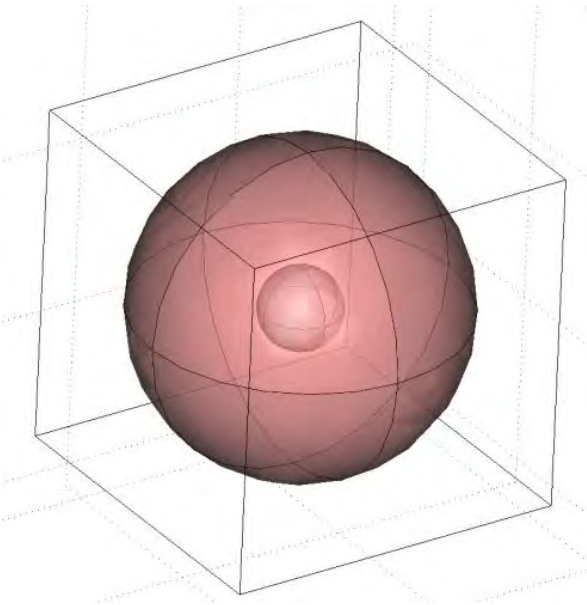


Figure 2.27: Core-Shell Structure

$$r_{core} = 0.25r_{shell}$$

$$\epsilon_{shell} = 29.23$$

$$\epsilon_{core} = 1 - 3 \frac{4.387^2}{(k_0 a)^2}$$

$$\mu_{core} = \mu_{shell} = 1$$

$$dx = dy = dz = 2.1a$$

We expect to achieve a strong electric response from the plasmonic sphere, as was achieved in the previous configurations. Furthermore, we hypothesize that the lossless dielectric shell will serve to circulate currents, inducing a magnetic dipole moment and thus a magnetic response. By setting the shell permittivity to  $\epsilon_{shell} = 29.23$  we hope the electric flux density will be sufficiently strong enough to induce this desired response.

## Results

The resulting dispersion curves are shown below in figures Figure 2.28 and Figure 2.29.

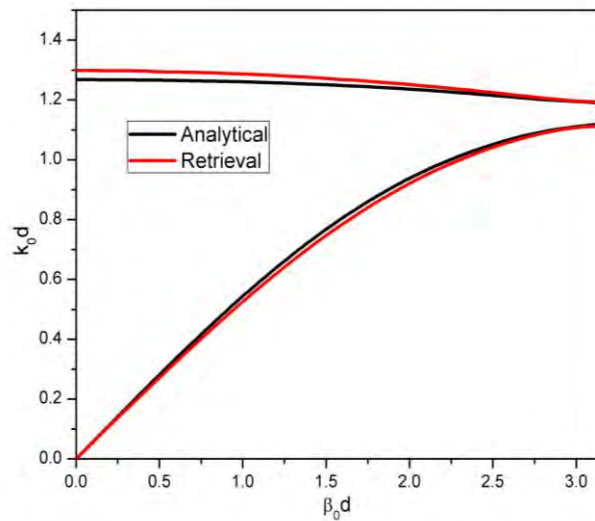
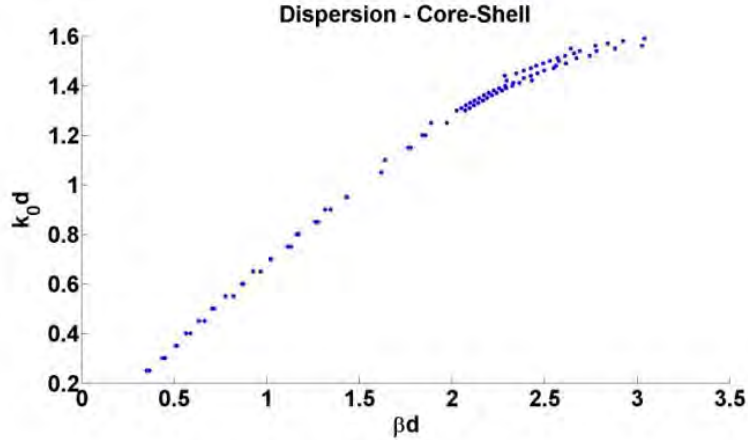


Figure 2.28: Analytical Dispersion Curve – Core-Shell Structure



**Figure 2.29: COMSOL Dispersion Curve - CoreShell Structure**

The analytical results demonstrate backward wave behavior for  $1.2 < k_0 d < 1.3$  in the second frequency band. The computational results, however, have been unsuccessful at retrieving the same band. In fact, it is curious to note that the results do not match. The analytical calculation values of  $k_0 d$  do not match the rigorous computational result.

Pending further study, we are forced to conclude that this core-shell structure is ineffective at supporting backward wave propagation, and does not act as a metamaterial for the parameters studied. It is left to analyze the electric and magnetic field distributions during simulation to determine if it does in fact exhibit the desired magnetic response.

## E. Conclusions

This chapter presents the implementation of a computational solver, linking COMSOL with MATLAB, that extracts metamaterial properties, such as dispersion diagrams, from a given geometry. We include a discussion on the equation that this platform solves and include its verification using known geometry dispersion diagrams.

We then apply this platform to study plasmonic spheres arranged isotropically, in linear chains, and in planar arrays. For the plasma frequency used, this work found that plasmonic spheres in linear chains and planar arrays function as metamaterials, while isotropic sphere arrangements do not. Furthermore, this research encourages further investigation into core-shell structures since the analytical results do not match the rigorous computational method.

## Chapter 3 METAMATERIAL GEOMETRY GENERATION (Sandia National Laboratories)

### A. Intro/Motivation

As has been stated and shown, a major challenge in metamaterial structural design is determining the relationship between a potential geometry and its bulk material response. Homogenization, dispersion analysis, and simulations are used to help determine this relationship.

In general, engineers and scientists approach this problem from the forward direction. We'll heuristically conceive of a potential geometry (i.e. plasmonic sphere arrangements or core-shell structures), create models of it, and run simulations on it to extract its material parameters.

What if we could do the inverse? Suppose we needed a metamaterial that satisfied some pre-determining conditions on effective permittivity and permeability, or that followed a given dispersion curve – how can we generate this metamaterial?

When it comes to some metamaterial applications we must engineer extremely non-homogenous distributions of unit cells. One such example is a coordinate transformation, which makes radiation "see" a space which is twisted, forcing EM waves to travel through it differently. Instead of an infinite periodic array of the same unit cell, we must find a metamaterial with spatial variations in  $\epsilon$  and  $\mu$ . Coordinate transformations of space can be mimicked by coordinate transformations of  $\epsilon$  and  $\mu$  [5], but with a high degree of nonlinearity.

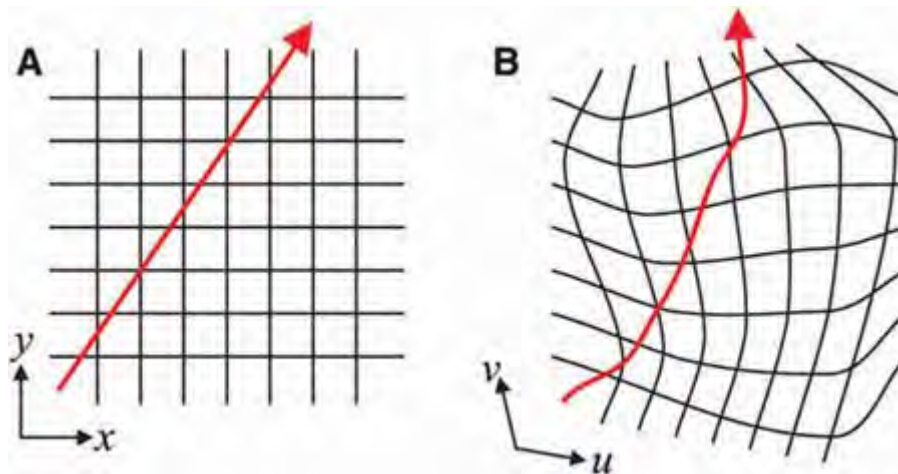


Figure 3.1: Transformation Optics - transforming a coordinate system [5]

For an arbitrary transformation it is next to impossible to determine the unit cell that needs to be used at every individual point, for each point will likely be different.

A research group at Sandia National Labs became interested in this sort of problem. In particular, they are interested in metamaterial generation at infrared (IR) frequencies.

We provide in this chapter a method by which this can be accomplished. We begin by an introduction and discussion of evolutionary algorithms – algorithms which have been shown to be effective at solving highly non-linear problems. They each take points in some parameter space and find the global optimum based on a fitness function  $F : \{parameter - space\} \rightarrow \mathbb{R}$ . Next we demonstrate how a metamaterial geometry can be converted from a geometry to a point in such a parameter space. Finally, we show some preliminary results in metamaterial evolution and discuss the next steps that need to be taken to convert this work into a fully automated metamaterial geometry generation system.

## B. Evolutionary Algorithms

Evolutionary algorithms are generic, population based, metaheuristic optimization algorithms. They mimic natural processes and simulate the way nature finds the “best fit” or “point of lowest energy” in a variety of scenarios. Potential solutions to a given problem serve as individuals of a population, and the fitness function determines their degree of optimization of each individual relative to a global maximum. By mutating and combining individuals and iterating many times over, the algorithms slowly converge on the global maximum.

The parameter space represents every possible individual that can exist. Take, for example, all permutations of eight letters. We may define a parameter space composed of all possible eight letter permutations and thus an individual in this space would be one permutation of the  $26^8$  different choices.

The fitness function represents a figure of merit of how close an individual is to the desired global maxima. In this example, we may define our fitness function to be related to the hamming distance to the word ‘material’. Then a permutation such as ‘maturiel’ would have very high fitness whereas a permutation like ‘pokenvkg’ would have very low fitness.

The algorithm then takes individuals and alters them in the hope of improving their fitness. By iterating this process the algorithm converges towards the global maximum. It may stop after a certain number of iterations or when an individual is within an allowable error of the global maximum.

We present two algorithms – the Genetic Algorithm and Simulated Annealing – which were used in this research to optimize metamaterial geometries.

### Genetic Algorithm

The genetic algorithm (GA) is inspired by Darwinian natural selection. According to Darwin, a species’ population survives if its members are sufficiently fit to live long enough to reproduce, ensuring the creation of a new population. Over time, the species will maintain its more desirable characteristics since fitter members are more likely to survive and reproduce. The genetic algorithm follows this. It is composed of a parameter space, a population of individuals, and a fitness function.

A population of individuals, dubbed chromosomes, is created within a prescribed parameter space. The size of this population is usually large in order to get the best genetic mix.

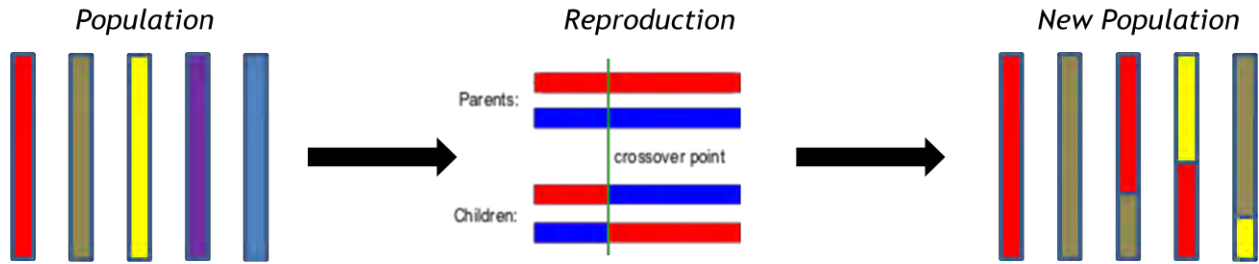


**Figure 3.2: Diagram of Genetic Algorithm Evolution**

Each individual is tested by the fitness function and the fittest members are then chosen to breed together to generate the next population. This is an algorithm design choice and is typically a fairly elite percentile – 10-15% of the top.

The method used for breeding is also a design choice, but in general is composed of crossover and mutation.

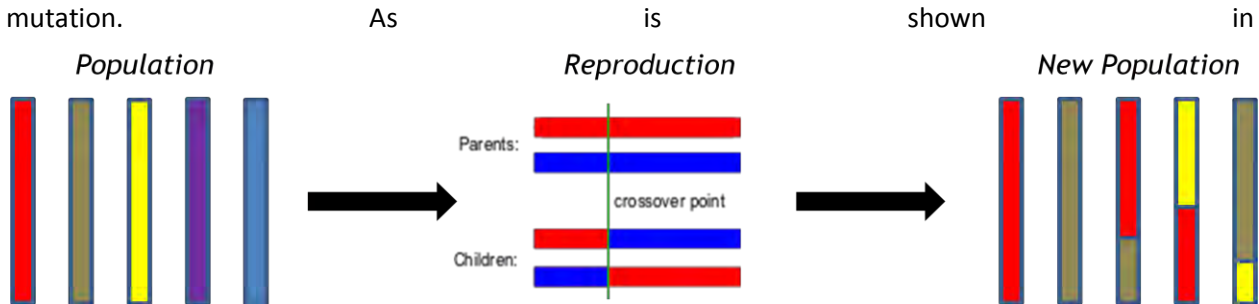
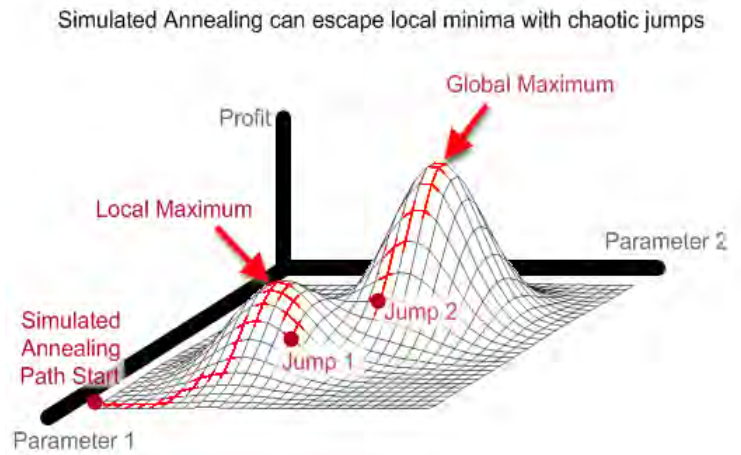


Figure 3.2 a crossover point is chosen to split two chromosomes whose remaining parts are then interchanged to form two members of the next population. Shown above is one-point crossover. This may be extended to multiple point crossovers if it improves the effectiveness of the algorithm. In addition, the top percentile (1%) of this already elite group is chosen to survive untouched to the next population in order to preserve the best members of the parameter space.

### Simulated Annealing

As the name implies, this algorithm simulates metallurgical annealing. This is the process by which a piece of metal is heated to a high temperature and slowly cooled in order to strengthen it. When the metal is heated its atoms become unstuck and wander around the material. As it slowly cools the atoms find states of lower energy, form larger crystals, and strengthen the metal. The slow cooling prevents atoms from ending up in local maxima, as is shown in Figure 3.3. The extended time that an atom would remain in local maxima gives it an increased probability of ‘jumping’ out of it, and ending up in the global maximum.



**Figure 3.3: Local Maxima in a parameter space** (<http://www.stanford.edu/~hwang41/>)

Simulated annealing follows this natural process. It takes a candidate solution (or potentially a series of candidate solutions) and increases their internal temperature. The probability that a candidate solution moves to a different point in the parameter space is a function of this internal temperature as well as the fitness value of each point, itself and the point in consideration. This causes the candidate solution to move around the parameter space with ever-decreasing probability until it is fully cooled and can no longer move. In particular, the probability of transitioning follows a Gaussian curve:

**3.1**

$$\mathbf{P}(f, f', T) = e^{\left(\frac{-|f' - f|}{T}\right)}, f' < f$$

$$\mathbf{P}(f, f', T) = 1, f' > f$$

Where  $f$  is the current fitness level,  $f'$  is the fitness level of the proposed transition point, and  $T$  is the internal temperature. Initially the probability of transitioning, even to a state of lower fitness, is rather high, allowing the candidate solution leeway to sweep across the parameter space in large bounds. As temperature decreases the probability of transitioning becomes very low for large values of  $|f' - f|$ , restricting movement to points very near the initial solution.

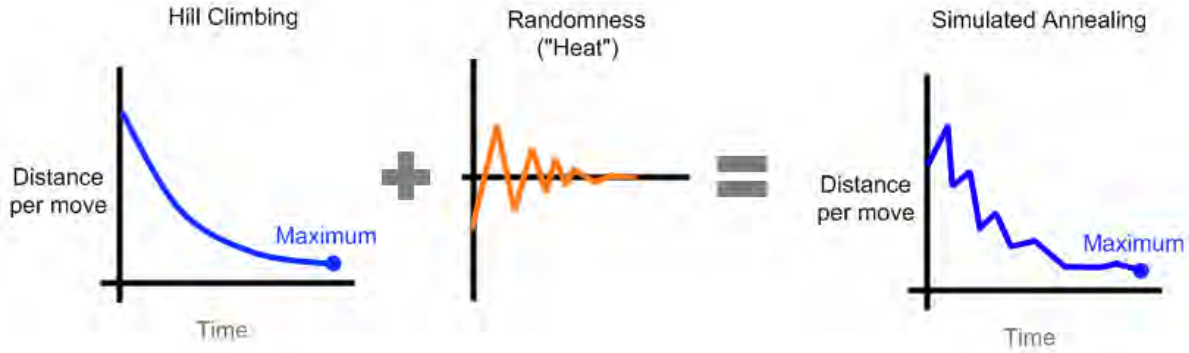


Figure 3.4: Randomness of Transitioning in Simulated Annealing

### C. Geometry Representation in Parameter Space

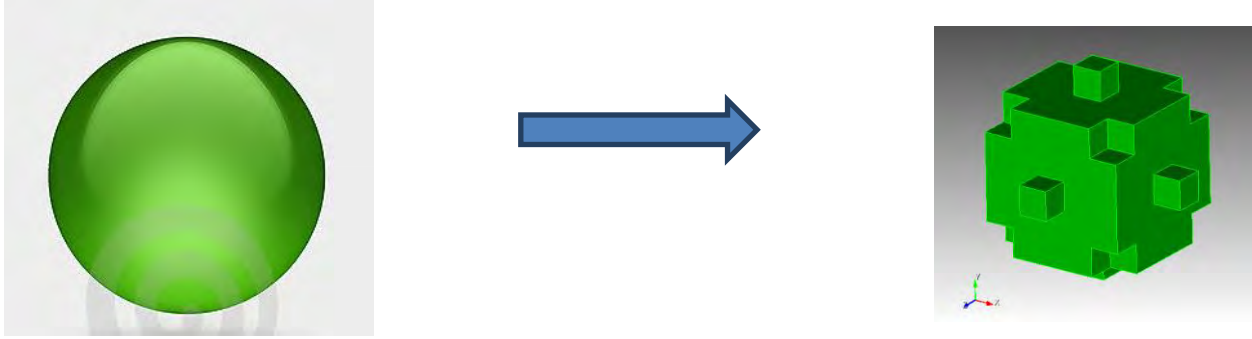
In order to effectively use these evolutionary algorithms, we must first convert our metamaterial geometries into forms which may be manipulated by them. Specific metamaterial geometries such as SRRs have been previously optimized using these sorts of algorithms [16]. However, this work has been largely constrained to pre-determined geometries, where the researchers are seeking some small improvement on existing functionality.

In this work we are interested in being able to generate a new unit cell. We do not seek to optimize an existing one. As a result, we must conceptualize a fairly large parameter space which encompasses a wide-enough range of metamaterial unit cells to be of interest in an automation procedure.

In consideration of the chosen optimization algorithms, we must choose a parameter space and unit cell representation which may be mutated, perturbed, and genetically recombined. In effect, we need to be able to decompose a unit cell into a chromosome, for the genetic algorithm, or a point in some general parameter space, for the simulated annealing algorithm.

We thus take a unit cell and pixilate it, much the way a digital picture pixilates a visual image. Starting from a 3D cubic cell, we pixilate it into  $n \times n \times n$  smaller cubes (dubbed cubons), creating a grid. We then consider each cubon to contain a two-dimensional space representing values of relative permittivity and permeability (i.e. each cubon contains a copy of  $\mathbb{R}^2 = \{\epsilon\} \times \{\mu\}$ ). This effectively creates a point in a  $2n^3$ -dimensional space. This point is represented by a  $n^3 \times 1$  vector where each entry is a point in  $\mathbb{R}^2 = \{\epsilon\} \times \{\mu\}$ .

We can see this pixilation graphically in Figure 3.5 using the meshing software Cubit - courtesy of Sandia National Labs. Here we see a unit cell containing a simple dielectric sphere pixilated into its parameter-space representation with  $n = 10$ . The figure makes evident the loss of detail that can arise with such a pixilation. We account for this in our simulations by maintaining a quasi-static limit on the unit cell. Therefore, if the wavelength is at least 10 times longer than the unit cell, even a rough pixilation like  $n=10$  results in very tiny details relative to the wavelength.



$$((\epsilon_{r,1}, \mu_{r,1}), (\epsilon_{r,2}, \mu_{r,2}), \dots, (\epsilon_{r,1}, \mu_{r,1}))$$

**Figure 3.5: Unit Cell Pixilation**

The greater the value of  $n$ , however, the greater the computational power needed to compute with these algorithms. For simple comparisons we may take  $n = 10$ , as shown here. For rigorous and more exact computation we let  $n$  go as high as 30.

This decomposition of a unit cell into a vector allows it to be manipulated by the algorithms. We can easily pass this vector as a chromosome to the GA. Similarly, any single vector can be thought of as a point in a  $2n^3$ -dimensional parameter space which may be used in an annealing algorithm.

#### **D. Geometry Evolution**

With our parameter space derived and our unit cells decomposed into vectors, we can now begin to apply these algorithms.

The first step is to show proof of concept. We must demonstrate that these algorithms are effective within such a parameter space.

#### **Fitness Functions – Shape Morphing**

In order to demonstrate initial functionality of these algorithms, we apply a simple fitness function. Instead of attempting to create a viable metamaterial, we take a geometry and attempt to morph it into another.

We define the Euclidean distance from one geometry to another to be the Euclidean distance from their respective vector representations. That is, if we define two unit cell shapes and convert them to vector form as

$$v_2 = ((\epsilon_1^2, \mu_1^2), (\epsilon_2^2, \mu_2^2), \dots, (\epsilon_n^2, \mu_n^2))$$

$$v_1 = ((\epsilon_1^1, \mu_1^1), (\epsilon_2^1, \mu_2^1), \dots, (\epsilon_n^1, \mu_n^1))$$

then their Euclidean distance is

### 3.3

$$D(v_1, v_2) = \sum_{i=1}^{n^3} \sqrt{(\varepsilon_i^1 - \varepsilon_i^2)^2 + (\mu_i^1 - \mu_i^2)^2}$$

where  $n$  is still the cubon pixilation and a superscript denotes labeling, not raising to a power.

We now have a metric which we can use to gauge one unit cell's "proximity" to another. In order to run our algorithm and get one inclusion to morph into another, the procedure now becomes simple. We let  $v_2$  be the vector form of the initial geometry. We let  $v_1$  be the vector form of the desired geometry. We then define the fitness function to be the distance function  $D$ , with  $v_2$  having higher fitness than  $v_3$  if  $D(v_1, v_2) < D(v_1, v_3)$ .

Figure 3.6 below shows the results of this sort of fitness function. In this example we let  $v_1$  be the union of two cylinders and  $v_2$  be a simple sphere. In addition, for demonstrative purposes, we restrict the relative permittivity to the discrete values of 1 and 2 (i.e. no electric response or weak dielectric) and we further restrict the relative permeability to 1 (i.e. no magnetic response). Thus, the presence of a colored cubon in Figure 3.6 represents a dielectric, and the absence of a cubon represents free space. This allows us to clearly visualize what is happening; otherwise the results would appear to be little more than solid cubic blocks of color.

By applying the simulated annealing algorithm to these geometries we observe the morphing of  $v_2$  into  $v_1$ . The temperature of the simulation starts at a high value, making the probability of transition from one vector to a neighboring vector almost 1. As a result, the first several hundred iterations tend to "melt" the structure, as can be seen below. The cubons appear to be scattering all over the unit cell. In reality, what is happening is that cubons are alternating between values for free-space and for dielectric material. The temperature cools, and as it does, the vector  $v_2$  slowly starts to take the form of  $v_1$ . By the third image in the series, we can already begin to discern a double cylinder, and by the final image in the series  $v_2$  is almost identically the double cylinder  $v_1$ , with a small error shown as the remaining free-floating cubons.

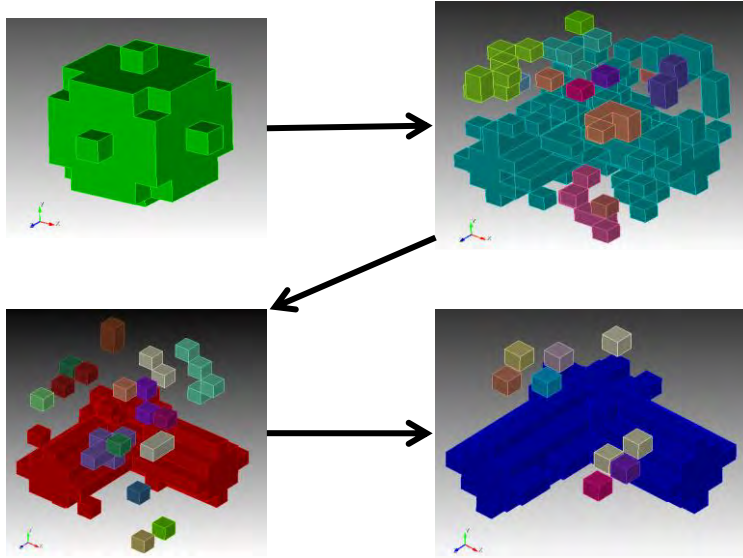


Figure 3.6: Simulated Annealing - Morph to Shape

### Fitness Functions – Metamaterial Generation

The next step in this research is the use of a metamaterial generation fitness function. We need to be able to extract the effective permittivity and permeability, the electric and magnetic polarizabilities, or the electric and magnetic far-field patterns (FFP) from a given geometry. Given any of those we may calculate the other two, so they are equivalent as far as fitness functions are concerned.

The Sandia Labs’ software Eiger is useful for calculating the FFP. It takes a meshed geometry from software such as Cubit, impinges a plane wave on it at a user-specified frequency, calculates the surface currents and the electric near-field, and propagates this field to the far-field using a harmonic green’s function.

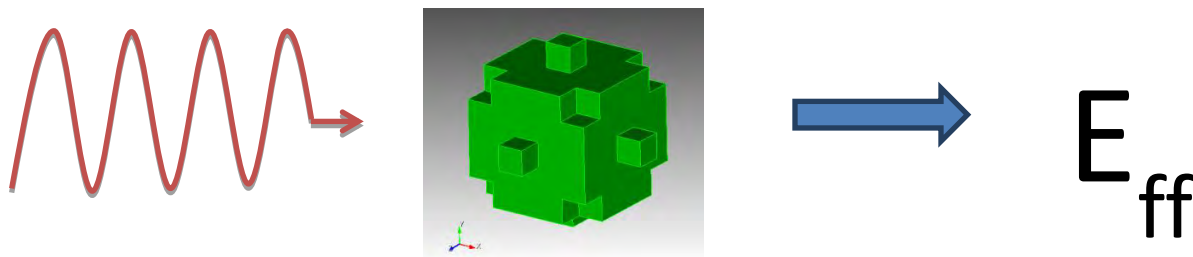


Figure 3.7: Eiger - Computational Far-Field solver

This software can thus be used as part of a fitness function. Given a desired FFP, we may define a fitness function to be the proximity of a unit cell’s FFP to this desired FFP. In essence we are grading a unit cell on how closely its material response resembles the desired material response. For this work, the fitness function was mapped as  $F : \{parameter - space\} \rightarrow [-\infty, 1]$  where 1 denotes a perfect match and the fitness function can take on negative values.

The first trials for simulated annealing achieved a best fitness value of 0.231. The algorithms would achieve their max and remain in the neighborhood of it for the rest of the iterations. This is an interesting result and hints at the fact that the local minima in this parameter space may be very deep. That is, once a point in the parameter space enters one of these local minima, it may require too large of a jump to be able to exit it.

We are currently running trials using the genetic algorithm and expect better results. The fact that the genetic algorithm works with a population of vectors means that even if certain individuals become stuck in deep local maxima, other individuals may converge on the global maximum. Furthermore we are running more trials with simulated annealing, varying the annealing parameters such as the cooling schedule in order to determine if we can converge on better solutions.

In addition, we are seeking supercomputing resources to more efficiently run these scenarios. The large parameter space and computational electromagnetic fitness function (i.e. Eiger) require extensive computational speed.

To better optimize our results, we are investigating the use of different EM solvers. The fact that Eiger is a surface solver makes it efficient at solving for the far field for a single trial. Effectively, it generates an enormous matrix (as a function of the geometry) and solves it for the FFP. However, since our method requires small perturbations of an initial geometry, it would be ideal to find a solver which populates a matrix and then perturbs it according to the change in geometry. Doing so would result in a much faster computational solver. For the time being, however, we are seeking fast method-of-moments (MoM) or finite-element-method (FEM) solvers which could be controlled by an external driver such as a C++ program.

Our end goal is a fully-automated computational platform capable of taking as input desired bulk material parameters and generating a metamaterial geometry that yields those parameters at a given frequency.

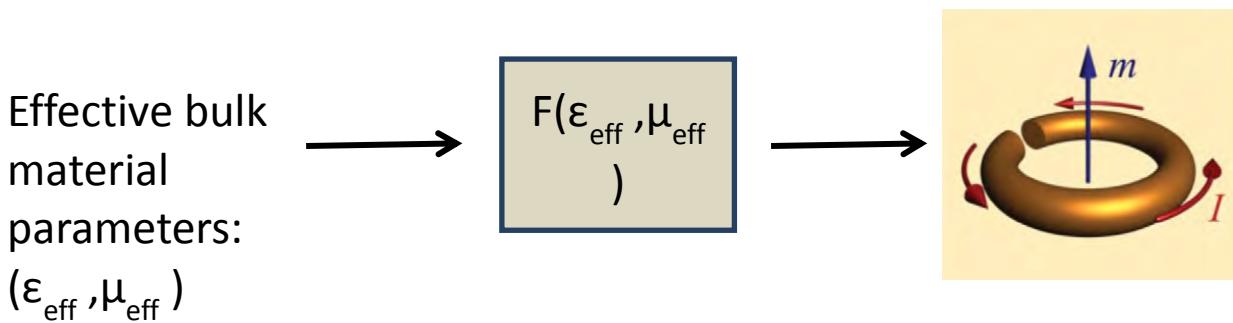


Figure 3.8: Computational Solver - Material properties to metamaterial geometry

## E. Conclusions

We present a potential solution for taking the desired bulk EM material response of a metamaterial and generating a geometry to yield those parameters.

This section contains an overview of two evolutionary algorithms – the genetic algorithm and simulated annealing – which describes the motivation and interest in working with these algorithms for optimization of a fitness function within a large parameter space. This is continued by describing the mapping of a metamaterial geometry to a point in a derived multi-dimensional parameter space. We then define a fitness function used for preliminary testing of the algorithms and show initial results. Finally, we describe the fitness function to be used for EM metamaterial generation and discuss initial findings, pointing to ways in which this process could be improved.

This work has succeeded in establishing a baseline computational platform for metamaterial generation. The infrastructure is established for this project, and what is left to do is to select a better EM solver to achieve better results.

## Chapter 4 Future Work/Conclusions

### A. Analysis of Conjugate SRRs using COMSOL/MATLAB Platform

The work at UT-Austin will continue. The COMSOL/MATLAB platform will now serve to test and analyze new metamaterial structure and rigorously characterize their EM response. In particular, the group would like to continue work on dual split ring resonators, as below.

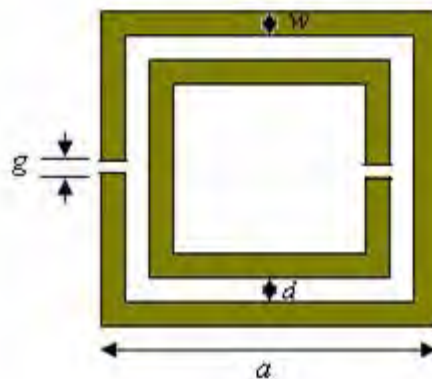


Figure 4.1: Dual Split-Ring Resonator ([http://www.microwaves101.com/encyclopedia/metamaterials\\_NITT.cfm](http://www.microwaves101.com/encyclopedia/metamaterials_NITT.cfm))

### B. Automated Metamaterial Geometry Generation

The work at Sandia National Laboratories will also continue. As described in the preceding sections, trials will continue to be run, varying the evolutionary algorithm parameters, in attempts to converge on better solutions. Furthermore the group is looking into the use of supercomputing resources to be able to run these long simulations in a shorter time frame. In addition, we will use a method-of-moments or finite-element-method solver to replace the surface solver currently in use.

### C. Conclusions

We present in this work the implementation of a bi-directional computational platform for metamaterial analysis and design.

$$(\epsilon_{\text{eff}}, \mu_{\text{eff}}) \longleftrightarrow$$

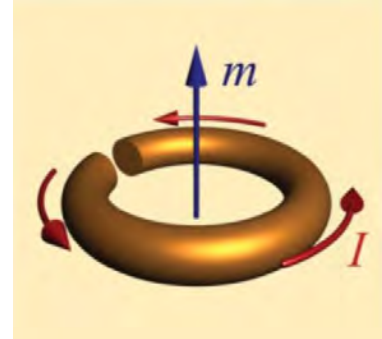


Figure 4.2: Bi-directional Platform for Metamaterial Design and Analysis

The work at UT-Austin developed a COMSOL/MATLAB interface which allows researchers to create a metamaterial unit cell and extract bulk material parameters from it. Using COMSOL we may define a geometry and specify the frequency ( $\omega$ ) of an impinging wave. Using an eigenvalue solver that solves a weak-field expression derived in the preceding sections, COMSOL calculates the propagating wavenumbers ( $\beta$ ) in the material. We may then extract the field distributions for any given ( $\omega, \beta$ ) pair. We can further use MATLAB to drive COMSOL in a frequency sweep to obtain a dispersion diagram. This platform was used to investigate plasmonic sphere arrangements and core-shell structures as viable optical-frequency metamaterials. The plasmonic spheres were arranged in three scenarios – isotropic, linear chains, and planar arrays. For the plasma frequency used, we found that the linear chain and planar array scenarios support backward-waves within a certain bandwidth while the isotropic case does not. The core-shell structure requires further investigation due to a discrepancy between the analytical and computational results. The analytical implies the presence of backward waves in the second band, while the computational does not.

The work at Sandia National Laboratories developed evolutionary algorithms for creating a unit cell geometry whose EM response satisfies given desired material parameters. We show the mapping of a metamaterial geometry into a corresponding vector representation in a large parameter space and demonstrate how this vector can be manipulated by the evolutionary algorithms. We then demonstrate the evolution of such a geometry-vector into a desired geometry-vector using a simple fitness function. We continue with the results obtained when using an EM-solver fitness function to attempt to morph a unit cell geometry into an actual metamaterial. We discuss the setbacks encountered as well as how to overcome them using faster EM-solvers. We conclude that further work is required before this part of the platform can be used for metamaterial generation

## References

- [1] V.G. Veselago, "The electrodynamics of substances with simultaneously negative values of  $\epsilon$  and  $\mu$ ," *Sov. Phys. Usp* 10, pp. 509-514, 1968.
- [2] Craig F Bohren and Donald R. Huffman, *Absorption and Scattering of Light by Small Particles.*, 1998.
- [3] J.B. Pendry, "Negative Refraction Makes a Perfect Lens," *Phys. Rev. Lett.*, pp. 3966–3969, 2000.
- [4] Schurig et al., "Metamaterial Electromagnetic Cloak at Microwave Frequencies," *Science*, vol. 314, no. 5801, pp. 977-980, Oct. 2006.
- [5] J. Pendry, D. Schurig, and D. R. Smith, "Controlling Electromagnetic Fields," *Science*, vol. 312, no. 5781, pp. 1780-1782, May 2006.
- [6] Andrea Alu and Nader Engheta, "Achieving transparency with plasmonic and metamaterial coatings," *Phys. Rev. E*, vol. 72, no. 016623, 2005.
- [7] Andrea Alu, "First-principles homogenization theory for periodic metamaterials," *Phys. Rev. B*, vol. 84, no. 075153, 2011.
- [8] R.A. Shelby, D. R. Smith, and S.C. Nemat-Nasser, S. Schultz, "Microwave transmission through a two-dimensional, isotropic, left-handed metamaterial," *Applied Physics Letters*, vol. 78, no. 4, 2001.
- [9] Chris Fietz, Yaroslav Urzhumov, and Gennady Shvets, "Complex k band diagrams of 3D metamaterial/photonic crystals," *Optics Express*, vol. 19, no. 20, pp. 19027-19041, 2011.
- [10] K. Sakoda, *Optical Properties of Photonic Crystals.*: Springer, 2004.
- [11] A. Pors, I. Tsukerman, and S. I. Bozhevolnyi, "'Effective constitutive parameters of plasmonic metamaterials: a," *arXiv*, vol. 1104.2972v1, 2011.
- [12] Kittell Charles, *Introduction to Solid State Physics*. New York City: Wiley, 1996.
- [13] Carlos A. Esteva, "Setting up and solving for the magnetic field distribution of various modes inside a metamaterial unit cell with a spherical inclusion using an eigenvalue solver," Univ. of Texas - Austin, Austin, Documentation - contact andre.esteva@gmail.com 2011.
- [14] Constantine A. Balanis, *Advanced Engineering Electromagnetics.*: Wiley, 1989.
- [15] Andrea Alu and Nader Engheta, "Three-dimensional nanotransmission lines at optical frequencies: A recipe for," *Phys. Rev. B*, vol. 75, no. 024304, 2007.
- [16] V. Sreenivas, G. Sundaram D. Karthik, "Optimization of Ring parameters of Artificial Magnetic Resonators using Swarm," in *3rd International Conference on Electronics Computer Technology (ICECT)*, Kanyukumari, 2011.